PPARγ mediated enhanced lipid biogenesis fuels *Mycobacterium tuberculosis* growth in a drug-tolerant hepatocyte environment.

Binayak Sarkar[1], Jyotsna[1], Mohit Yadav[1], Priya Sharma[2], Raman Deep Sharma[2], Shweta Singh[3], Aakash Chandramouli[4], Kritee Mehdiratta[5], Ashwani Kumar[3], Siddhesh S. Kamat[4], Devram S. Ghorpade[1], Debasisa Mohanty[1], Dhiraj Kumar[2], Rajesh S. Gokhale[1,4,#].

1 Immunometabolism laboratory, National Institute of Immunology, New Delhi, India, 2 Cellular Immunology Group, International Centre for Genetic Engineering and Biotechnology, New Delhi, India 3 CSIR-Institute of Microbial Technology, Chandigarh, India, 4 Indian Institute of Science Education and Research, Pune, Maharashtra, India.5 Council Of Scientific and Industrial Research–Institute of Genomics and Integrative Biology (CSIR-IGIB), New Delhi 110025, India, Academy of Scientific and Innovative Research (AcSIR), Ghaziabad 201002, India

Current address: Indian Institute of Science Education and Research, Pune, Maharashtra, India.

Keywords: Liver, Mtb, hepatocytes, PPARγ, anti-TB drugs, lipid droplets.

Corresponding author: Rajesh S. Gokhale (rsg@nii.ac.in)

Abstract

Mycobacterium tuberculosis (Mtb) infection of the lungs, besides producing prolonged cough with mucus, also causes progressive fatigue and cachexia with debilitating loss of muscle mass. While anti-tuberculosis (TB) drug therapy is directed toward eliminating bacilli, the treatment regimen ignores the systemic pathogenic derailments that probably dictate TB-associated mortality and morbidity. Presently, it is not understood whether Mtb spreads to metabolic organs and brings about these impairments. Here we show that Mtb creates a replication-conducive milieu of lipid droplets in hepatocytes by upregulating transcription factor PPARγ and scavenging lipids from the host cells. In hepatocytes, Mtb shields itself against the common anti-TB drugs by inducing drug-metabolizing enzymes. Infection of the hepatocytes in the *in vivo* aerosol mice model can be consistently observed post-week 4 along with enhanced expression of PPARγ and drug-metabolizing enzymes. Moreover, histopathological analysis indeed shows the presence of Mtb in hepatocytes along with granuloma-like structures in human biopsied liver sections. Hepatotropism of Mtb during the chronic infectious cycle results in immuno-metabolic dysregulation that could magnify local and systemic pathogenicity, altering clinical presentations.

Introduction

Mycobacterium tuberculosis (Mtb), the causative agent of human tuberculosis, remains the leading infectious killer globally with an estimated death of 1.3 million in 2022[1]. Despite progressive work on designing new anti-TB therapeutics and implementing vaccination programs in TB-endemic countries, it has a high global case fatality rate and a poor treatment success rate, along with a rising number of drug-resistant infections[2, 3]. Emerging paradigms in infectious diseases advocate tackling pathogen-driven ailments as one-dimensional problems, where the entire emphasis is given to pathogen elimination. A holistic understanding of how the host systems respond to the infection, vaccination, and treatment is key to TB management programs[4]. Recent widespread and severe physiological derangements associated with COVID-19 patients, even after

56 the elimination of the virus, have brought back the focus on identifying novel strategies
57 that are inclusive of modulating the host immune-metabolic axis[5, 6].

58 The clinical symptoms of pulmonary TB encompass localized manifestations like
59 prolonged cough with mucus, pleuritic chest pain, hemoptysis, and lung damage.
60 Besides, systemic outcomes like cachexia, progressive fatigue, oxidative stress, altered
61 microbiota and glucose intolerance result in organ-wide disruptions[7, 8]. Pulmonary TB
62 patients often suffer from progressive and debilitating loss of muscle mass and function
63 with severe weight loss, this TB-associated cachexia cannot be reversed by conventional
64 nutritional support[9, 10]. Besides, numerous epidemiological studies indicate that
65 hyperglycemia may occur during active tuberculosis, which can compromise insulin
66 resistance and glucose tolerance, although the mechanisms are unclear[7, 11, 12]. Both
67 the localized and systemic pathophysiology of TB infection indicate an alteration in the
68 host immuno-metabolic axis. It is somewhat bewildering that the engagement of the liver
69 during the Mtb infection cycle is not considered, despite its central role in balancing the
70 immune and metabolic functions of the body[13]. The crosstalk between the liver and lung
71 has been largely overlooked in tuberculosis (TB), even though acute phase proteins
72 (APPs) are used as predictive biomarkers in pulmonary tuberculosis[14]. A robust hepatic
73 APR response in mice, mediated by key hepatocyte transcription factors, STAT3 and NF-
74 κB/RelA, has been known to trigger pulmonary host defenses for survival during
75 pneumonia and sepsis[15]. In TB, the active phase of the disease is associated with
76 heightened expression of various genes that modulate flux in the lipid metabolic
77 pathways[16-18].

78 The liver is involved in a wide variety of functions – synthesis of plasma proteins, secretion
79 of various hepatokines, degradation of xenobiotic compounds, and storage of lipids,
80 glucose, vitamins, and minerals[19, 20]. De-novo lipogenesis, secretion of acute phase
81 proteins, hepatokine production, etc. are all directly or indirectly controlled by the
82 hepatocytes, thereby communicating with almost all the organs of the body[19, 21].
83 Moreover, the liver is actively involved in triacylglycerol synthesis and storage under the
84 intricate regulation of various hormones like insulin, glucagon, and thyroid hormone[22].
85 All these functions uniquely position the liver as the central regulator of lipid metabolism.

86 To avert organ damage, the liver maintains tolerogenic properties rendering it an attractive
87 target for various pathogenic microorganisms. Although several studies have indicated
88 the role of both -Mtb virulence components and host factors (immune activation, nitric
89 oxide, IFNγ, intracellular pH and hypoxia) in the generation of Mtb drug tolerance, the role
90 of liver, being the principal center for xenobiotic metabolism needs careful
91 investigation[23-27]. Liver is the hub of both phase I and phase II drug modifying enzymes
92 (DMEs). The levels as well as the activity of both type of DMEs play significant roles in
93 determining the pharmacokinetics and efficacy of various drugs across multiple diseases,
94 from infection to malignancy[28].

95 In this study, we demonstrate the active involvement of the liver in a murine aerosol TB
96 infection model during the chronic phase and establish hepatocytes as a new replicative
97 niche for Mtb. Using a variety of *in vivo*, *ex vivo*, and *in vitro* techniques we show how Mtb
98 perturbs biological functions within hepatocytes remodeling intracellular growth,
99 localization, and drug sensitivity. Cellular and mass spectrometric studies demonstrate
100 Mtb infection-mediated enhanced fatty acid biogenesis and TAG biosynthesis in the
101 hepatocytes regulated by PPARγ. We propose that infection of hepatocytes by Mtb during
102 the chronic phase can contribute to significant changes in disease progression, TB
103 treatment, and development of infection-induced metabolic diseases.

104 **Results**

105 **Human miliary tuberculosis patients harbor Mtb in the liver**

106 Mtb infects lungs, and other organs like lymph nodes, pleura, bones, and meninges.
107 There are also isolated case reports of hepatic TB, without providing many
108 pathophysiological consequences[29, 30]. To gain further insights into the involvement of
109 the liver in Mtb infections, we acquired human autopsied liver samples from individuals
110 with miliary tuberculosis and analyzed them for the presence of Mtb bacilli. Hematoxylin
111 and eosin (H and E) staining showed the presence of distinct immune cell infiltration and
112 granuloma-like structures in the infected samples **(Fig 1A and Fig S1C).** We examined
113 the liver specimens, with Mtb specific Ziehl-Nielsen (Z-N) acid-fast and auramine O-
114 rhodamine B stain (**Fig 1B, C**). Both these stains showed distinct positive signals with
115 characteristic rod-shaped bacilli that could be visualized by the acid-fast staining (as

116 indicated by arrows) **(Fig 1B).** We further corroborated our findings by performing
117 fluorescence in-situ hybridization (FISH) using Mtb-specific 16s rRNA probes, where
118 specific signals were observed **(Fig 1D).** The specific staining in FISH eliminates the
119 possibility of non-tuberculous mycobacteria (NTMs) in the tissue specimen and confirms
120 the presence of Mtb infection in the liver. Similar staining in the uninfected liver sections
121 from other individuals did not show any signal. **(Fig S1 A, B**). Although hepatic granuloma
122 is the characteristic histological feature for both local and miliary forms of hepatic TB, the
123 precise involvement of the different cells like Kupffer cells, hepatocytes, stellate cell, liver
124 sinusoidal endothelial cells, hepatic stellate cells, and other cell types have not been
125 studied in detail[31]. Multiplex immunostaining with β-actin antibody and Mtb-specific
126 Ag85B antibody shows the presence of Ag85B signals within the human hepatocytes
127 further confirming the presence of Mtb within hepatocytes (**Fig 1E and Fig S1D)**,
128 indicated with yellow arrows). Hepatocytes are morphologically distinct, large polygonal
129 cells (20-30 μm) with round nuclei, many of which are double-nucleated and mainly
130 positioned at the center of the cytoplasm[32]. The presence of Ag85B signals near the
131 nucleus, as depicted in (**Fig 1E and S1 D)**, further supports our assertion. Moreover,
132 hepatic granulomas in the human samples showed localized clustering of the immune
133 cells **(Fig S1D).** The corresponding Ag85B staining in the uninfected liver biopsy samples
134 did not show any signal (Fig 1F). Furthermore, to establish a correlation between liver
135 Mtb load and Mtb burden at the primary infection site, the lung, we conducted H&E
136 staining and acid-fast staining on lung sections from the same individuals. H&E staining
137 revealed distinct granulomas, while acid-fast staining confirmed an elevated bacterial
138 load, both indicative of a high degree of infection **(Fig S1E, F).** Using auramine O-
139 rhodamine B, Ziehl-Nielsen acid-fast staining, and FISH, Mtb presence was detected in
140 several lung specimens **(Fig S1G).** These results indicate Mtb infection in the liver of
141 human subjects and suggest the localization of Mtb within hepatocytes. These findings
142 are quite intriguing considering very few studies have discussed the lung-liver cross talk
143 or the involvement of liver in pulmonary TB.

144

145 **Mtb infection of mice via the aerosol route leads to significant infection of the liver**
146 **and primary hepatocytes**

147 To investigate whether the liver harbours Mtb during mice aerosol infection, we infected
148 C57BL/6 mice with 200 CFU of Mtb *H37Rv* and scored for the bacterial load in the
149 conventional niche- the lung as well as in the liver. Mtb could be detected in the liver
150 consistently across several experiments at 4 weeks post-infection and the bacterial load
151 increased till week 10 **(Fig 2A and B).** Consistent with the Mtb burden, phalloidin and
152 hematoxylin and eosin (H and E) staining of the infected liver at 8 weeks post-infection
153 showed localized cellular aggregation forming ectopic granulomas forming a granuloma-
154 like structure **(Fig 2C and S2C).** Further staining the liver sections with CD45.2 antibody
155 shows clustering of immune cells in Mtb infected mice liver **(Fig S2D).** To assess whether
156 liver infection leads to deranged liver function in the aerosol model, we analyzed the levels
157 of liver functional enzymes like albumin aspartate transaminase (AST), alanine
158 transaminase (ALT), and gamma-glutamyl transpeptidase (GGT) in the sera. Till week 10
159 post-infection, sera levels of these markers showed significant alterations as the infection
160 progressed, especially in the levels of AST with changes also in the levels of albumin and
161 GGT **(Fig S2B).** Since hepatocytes, the principal parenchymal cells of the liver constitute
162 70-80 percent of the liver by weight, we hypothesized whether hepatocytes could harbour
163 Mtb in the murine model of infection. To this end, we isolated primary hepatocytes from
164 the mice at different time points post-infection. The purity of the isolated hepatocytes was
165 validated by multiple methods-morphologically hepatocytes can be identified by their
166 distinct hexagonal architecture, round nucleus, some of which are binucleated as
167 observed in Alexa fluor phalloidin 488 and DAPI stained hepatocytes **(Fig 2E).** Flow
168 cytometry staining with antibody against hepatocyte specific marker asialoglycoprotein
169 receptor 1 (ASGR1) protein, confirmed that almost 100 percent of the isolated cells are
170 primary hepatocytes as seen in **(Fig 2F)**. It was further validated by confocal microscopy
171 as all the cultured cells specifically stained for ASGR1 protein, although with variable
172 levels of expression **(Fig 2G).** After thorough confirmation of the identity and the purity of
173 the hepatocytes, the cells were lysed and plated. Like the whole liver CFU, Mtb infected
174 primary hepatocytes (PHCs) at 4 weeks post-infection with substantial bacterial load at
175 week 6 and week 8 **(Fig 2H).** Staining with antibody for Mtb-specific Ag85B protein in both

176 the infected tissue sections and cultured hepatocytes isolated from the *in vivo* infected
177 mice revealed the presence of Mtb within hepatocytes **(Fig 2D and 2I)**. To further
178 strengthen our data, we co-stained the isolated primary hepatocytes from the Mtb infected
179 mice with anti-albumin antibody (albumin is a robust and widely used hepatocyte marker)
180 and Ag85B. As depicted in (Fig 2J), distinct Ag85B signals can be observed in the albumin
181 rich hepatocytes. Besides the aerosol route, infection intraperitoneally also led to
182 hepatocyte infection, also led to hepatocyte infection as early as day 10 **(Fig**
183 **S2A).** Further, to prove the spread of Mtb to the liver in other model organisms, we
184 infected guinea pigs with 200 CFU of Mtb and analyzed the bacterial load in the lung,
185 liver, and spleen at week 4 and week 8 post-infection **(Fig S3A)**. At both the time points
186 we could observe robust liver infection with granulomatous structure in the liver, proving
187 that the dissemination of Mtb to the liver occurs across multiple model animals **(Fig S3B).**

188 **Hepatocytes provide a replicative niche to Mtb**

189 Consistent data from human TB patients and aerosol murine model prompted us to
190 develop an in vitro model of Mtb and hepatocyte infection. We examined Mtb infection in
191 several hepatocyte cell lines of mouse and human origin along with primary murine
192 hepatocytes. Infection studies with fluorescently labeled Mtb *H37Rv* were carried out with
193 primary murine hepatocyte cells (PHCs), HepG2, Huh-7, and AML-12 **(Fig 3A, B,**
194 **and C).** The multiplicity of infection was titrated both in PHCs and HepG2 with the MOI of
195 1, 2.5, 5, and 10. MOI 10 consistently showed an infectivity of more than 60% in both
196 HepG2 and PHCs **(Fig S4 A, B, and C).** While we acknowledge that MOI 10 is
197 moderately high, several well-cited studies have used MOI 10 for various conventional
198 phagocytes and other non-conventional cell types like mesenchymal stem cells,
199 adipocytes and human lymphatic endothelial cells[33-37]. Hence MOI 10 was selected
200 for further experiments. Macrophage cell lines RAW 264.7, THP-1, and mouse bone
201 marrow-derived macrophages (BMDMs) were used as positive controls. Even though
202 PHCs, HepG2, Huh-7, and AML-12 are not considered to be classical phagocytic cells,
203 all cells showed infectivity of more than 60 percent after 24 hours, comparable to RAW
204 264.7, THP-1 and BMDMs **(Fig 2A, B).** Analysis of bacterial load in the PHCs post-
205 infection showed colony-forming units (CFU) like RAW 264.7, THP-1, and BMDMs,

206 supporting microscopic observations **(Fig 3C).** Mtb in macrophages is known to remodel
207 the intracellular environment to survive within phagosomes. We studied Mtb growth
208 kinetics within hepatocytes using GFP-labeled Mtb *H37Rv* in PHCs and HepG2 **(Fig**
209 **3D and F).** Mean fluorescent intensity measurements showed a consistent increase in
210 GFP intensity in both PHCs and HepG2 with increasing time **(Fig 3E and G).** Fold change
211 in replication dynamics with respect to 5 hours post infection (HPI) showed that, while
212 bacterial growth in macrophages plateaus after 48 hours post-infection, Mtb continues to
213 grow in both HepG2 and PHCs **(Fig 3H**). Relative CFU numbers in the PHCs and HepG2
214 further supports our data (Fig S4 D-H). Our studies thus establish that hepatocytes,
215 besides being robustly infected by Mtb, also provide a favourable replicative niche for
216 Mtb.

217 **Transcriptomics of infected hepatocytes reveal significant changes in key**
218 **metabolic pathways**

219 To understand Mtb-induced changes in the hepatocytes and the underlying mechanisms
220 of how hepatocytes provide a favourable environment to the pathogen, we performed
221 transcriptomic analysis of the infected and sorted HepG2 cells at 0 hours (5 hours post
222 incubation) and 48 hours post-infection. Sorting before RNA isolation specifically enriches
223 the infected cellular population thus eliminating cellular RNA from uninfected cells **(Fig**
224 **4A**). Unsupervised clustering segregated the data into 4 distinct groups on the PC1 with
225 a variance of 27 percent, showing good concordance within the replicates **(Fig 4B).** The
226 close spatial clustering for the two 0-hour time points corresponding to uninfected and
227 infected is indicative of relatively less transcriptomic changes. On the other hand, the
228 spatial segregation of the 48 hours datasets suggests clear differences between the RNA
229 transcripts of uninfected and infected cells. The differentially expressed genes were
230 calculated using DE seqR with fold change >0.5 and a false discovery rate of <0.2. Gene
231 ontology (GO) enrichment analysis for the differentially regulated pathways at both the
232 early (0 hours) and the late (48 hours) infection time points is shown in **(Fig 4C).** At 0
233 hours post-infection, the immediate stress response pathway of the cell, involving ROS
234 generation, intracellular receptor signaling pathways, and response to xenobiotic stresses
235 got activated, while at a late time point, Mtb modulated some of the key immuno-metabolic

236 pathways like macroautophagy, cellular respiration, proteasomal degradation pathway,
237 response to type I interferon, IκB kinase/NF-κB signaling, etc **(Fig 4D).** Major alterations
238 in the vacuolar and vesicular transport at 48 hours are indicative of the dynamic changes
239 in the phagosome maturation pathway **(Fig 4D).** Volcano plot analysis showed greater
240 relative changes in the gene expression pattern at 48 hours compared to 0 hours, with
241 many genes like *CXCL10, CXCL11, IDO, CCL5* etc being greatly upregulated **(Fig 4E,**
242 **4F).** Interestingly, our RNA sequencing data indicated major changes in various facets of
243 lipid metabolic pathways like fatty acid biosynthesis pathway, glycerolipid and
244 glycerophospholipid metabolism, cholesterol biosynthesis pathways, etc. Several key
245 genes like *FASN, DGAT1, DGAT2*, *HMGCR*, etc. were upregulated, indicating the
246 possibility of greater synthesis of neutral lipids. Additionally, we have added a
247 supplementary excel file with top 1000 DEGs at both 0 hours and 48 hours post-infection.
248 Thus, transcriptomic studies shed light on several of the key Mtb-induced changes in the
249 hepatocytes.

250 To understand the difference and similarities between the pathways that get affected in
251 macrophages compared to hepatocytes during Mtb infection, we compared the gene
252 expression analysis data from Mtb-infected HepG2, 48 hours post-infection with THP-1
253 infected macrophages, 48 post-infection, taken from Kalam et al.,[35] **(Fig S5 A, B).** The
254 comparison provides insights regarding how Mtb modulates different pathways
255 depending on the type of the host cell infected. In THP-1, most of the altered pathways
256 are related to mounting an effective immune response to the bacteria like type 1 interferon
257 signalling pathway, regulation of cytokine secretion, leukocyte chemotaxis, response to
258 zinc, etc while in HepG2 the pathways that are getting altered are related to metabolism
259 like response to xenobiotic stimulus, macroautophagy, glycerophospholipid and
260 glycerolipid metabolism, and cellular respiration. This comparative analysis is indicative
261 of Mtb's ability to harness the metabolic richness of hepatocytes probably as a source for
262 nutrients. Moreover, being a non-immune cell type, hepatocytes might lack a robust innate
263 immune pathway like the macrophages and hence be less likely to clear mycobacterial
264 infections.

265

266 **Increased fatty acid synthesis drives Mtb growth in hepatocytes**

267 Mtb survival in foamy macrophages is driven by nutrient acquisition from the lipid
268 droplets[36]. Transcriptomic studies of Mtb-infected cells also showed upregulated
269 pathways for lipid metabolism. Examination of Lipid droplets in both PHCs and HepG2
270 revealed an increase in the number of lipid droplets at 24 hours post-infection **(Fig**
271 **5A and B).** Time kinetic analysis of BODIPY intensity in the infected HepG2 at different
272 days post-infection indicated a concomitant increase in lipid droplets with the progress of
273 infection **(Fig 5C).** Moreover, in PHCs, GFP labeled Mtb showed a high degree of
274 colocalization with the lipid droplets **(Fig 5D).** Lipid droplets are single membrane-bound
275 depots consisting mainly of neutral lipids like diacylglycerols (DAGs), triacylglycerols
276 (TAGs), and cholesterol esters (CEs)[38].

277 Mass-spectrometric analysis of the infected and uninfected HepG2 cells at 24 hours post-
278 infection, showed an increase in both TAGs and DAGs and CEs with a decrease in the
279 levels of free cholesterols, indicating Mtb-induced changes in the neutral lipid
280 biosynthesis **(Fig 5E).** To understand whether Mtb utilizes host lipid droplets as a source
281 of nutrients in hepatocytes, we treated Mtb-infected hepatocytes with specific inhibitors
282 of de-novo fatty acid biosynthesis (C75) and TAG biosynthesis (T863) **(Fig S6**
283 **A).** Interestingly, inhibiting both de-novo fatty acid biosynthesis as well as TAG
284 biosynthesis reduced the bacterial load in both PHCs and HepG2 by almost 1.0-1.5 log
285 fold **(Fig 5G and H)**. In THP-1 macrophage, although C75 reduced bacterial load by 0.5
286 log fold but T863 did not affect the bacterial load **(Fig 5I).** To get better insights into the
287 nutritional dependency of intracellular Mtb on hepatocyte lipid source, we metabolically
288 labelled HepG2 with 7.5 µg/ml of fluorescently tagged fatty acid (BODIPY 558/568 C_{12})
289 which subsequently accumulated into host lipid droplets. After 16-20 hours, the labelled
290 cells were treated with T863 and C75. Although T863 significantly reduced the load of the
291 intracellular TAGs, C75 had little effect on the level of accumulated TAGs and showed a
292 phenotype like the DMSO control **(Fig S6 C and D).** We infected these three set of cells
293 with Mtb (MOI:10) for 24 hours. The Mtb isolated from DMSO and C75 treated HepG2
294 became distinctly labelled with highly fluorescent lipid bodies, but the fluorescence signal
295 in Mtb derived from T863 treated cells was quite low and sparse **(Fig 5F and S7**

296 **A).** Considering that host-derived fatty acids are converted to triacylglycerols (TAGs) in
297 the bacterial cytoplasm as a source of carbon and energy, we wanted to check whether
298 the TAG synthesis machinery was modulated in the hepatocyte-infected Mtb. To this end,
299 we isolated Mtb from HepG2, 48 hours post-infection, and analysed for key genes
300 involved in TAG biosynthesis. Mtb grown in DMEM was used as a control.
301 Interestingly, *Tgs1, Tgs4, Rv 1760*, etc were upregulated by 6-8-fold, indicating an active
302 Mtb transcriptional change in Mtb to utilize and store host-derived lipids **(Fig S6**
303 **B).** Cumulatively, our studies thus demonstrate fatty acid biosynthesis and TAG formation
304 to be important for Mtb growth in hepatocytes.

305 To assess the status of the neutral lipids in the liver, BODIPY staining was conducted in
306 the liver cryosections of uninfected and infected mice (8 weeks post-infection). The liver
307 of Mtb-infected mice bears more lipid bodies **(Fig S8 A).** Co-immunostaining of BODIPY
308 and Ag85B also showed abundant lipid droplets and specific signals of Ag85B **(Fig S8**
309 **B).** Next, we stained the liver of Mtb-infected mice at 2-, 4- and 8-weeks post-infection
310 with LipidTOX neutral red dye. Surprisingly we found an elevated signal intensity of the
311 dye at 8 weeks post-infection. This shows that in mice, Lipid droplets might correlate with
312 Mtb burden **(Fig S8 C, D).** Our data comprehensively establishes infection-induced lipid
313 droplet accumulation as a pathogenic outcome of Mtb involvement in the liver during the
314 chronic stage of infection.

315 **PPARγ upregulation in Mtb-infected hepatocytes leads to augmented lipid**
316 **biogenesis**

317 To understand the molecular mechanism behind the accumulation of lipid droplets in the
318 Mtb-infected liver at 8 weeks post-infection, we investigated the expression patterns of
319 the transcription factors involved in the regulation of the genes of lipid biogenesis in our
320 RNA-seq data. At 48 hours post-infection, the transcript levels of Peroxisome proliferator-
321 activated receptor-gamma (PPARγ) were upregulated by 5-6-fold. To validate, that we
322 performed quantitative real-time PCR analysis of the *PPAR γ* gene in the infected HepG2
323 at 48 hours post-infection. With respect to the uninfected control, *PPAR γ* was
324 upregulated by 3-4-fold. Besides, downstream adipogenic genes that are directly or
325 indirectly controlled by *PPARγ* like *MGAT1*, *FSP27*, *FASN*, *DGAT1*, *DGAT2*, *ACAT1,*

326 *ACAT2, ADIPSIN* etc were all upregulated by more than 2-fold in the infected cells. **(Fig**
327 **S9 A).** Immunoblot also revealed a greater level of PPARγ protein in primary mouse
328 hepatocytes at 24 hours and 48 hours post-infection in the Mtb infected cells **(Fig 6C, D).**
329 In the in-vivo Mtb aerosol infection model, *Pparγ* expression levels showed an intriguing
330 trend, at week post-infection, the expression level was comparable to the uninfected
331 control, while at week 4 post-infection, the expression level spiked to 1.5-2-fold, reaching
332 3-4 fold at week 8 **(Fig 6B).** The pattern of expression of *Pparγ* in the infected liver
333 correlated with the bacterial load in the liver, where we see the induction at week 4 when
334 Mtb reaches the liver and maximum expression at week 8 when the load of Mtb is
335 considerably high. Besides, PPARγ, some of the critical enzymes involved in fatty acid
336 biosynthesis, TAG biosynthesis, cholesterol esterification like *Fasn, Dgat1, Dgat2, Mgat1,*
337 *Acat1, Acat2* etc showed a temporal increase in expression levels at the later time points
338 post-infection **(Fig 6A).** We then used a specific inhibitor of PPARγ, GW9662 (20 μM) and
339 agonist of PPARγ, rosiglitazone (20μM) in infected HepG2 and quantified the bacterial
340 load after 48 hours. Surprisingly, inhibition of PPARγ decreased the bacterial load by
341 almost 2-fold, while chemically inducing PPARγ increased the bacterial load
342 considerably **(Fig 6 E and F, and S9B)**. Moreover, LD number in cells also directly
343 correlated with the levels of PPARγ **(Fig 6G and H).** To investigate whether, PPARγ
344 expression was also induced in the liver of infected mice, we examined PPARγ in the liver
345 post infection. Interestingly, we found enhanced expression PPARγ in the liver of the mice
346 at 8 weeks post infection **(Fig S9 C and D).** Moreover, PPAR-γ intensity in hepatocyte
347 was also high in the infected liver **(Fig S9 E).** Thus, PPARγ activation resulting in lipid
348 droplets formation by Mtb might be a mechanism of prolonging survival within
349 hepatocytes.

350 **Hepatocyte resident Mtb displays a drug-tolerant phenotype**

351 The success of Mtb as a formidable pathogen depends on its ability to tolerate various
352 anti-TB drugs[39]. Drug tolerance is a phenomenom of Mtb surviving drug treatment of
353 longer durations in the absence of any resistance mechanisms. It is a property exhibited
354 by the bacteria but is influenced by both the host and the bacterial factors[23].
355 Interestingly, hepatocytes are a unique cell type that contain phase I and phase II drug

356 metabolising enzymes[40, 41]. The pharmacological potency of lipophilic drugs is
357 determined by the rate at which these drugs are metabolized to inactive products.

358 Cytochrome P450 monooxygenases (cyp450s) system is the key phase I DMEs and
359 known to interact with rifampicin[42]. We therefore analysed whether Mtb infection
360 influences the cyp genes in hepatocytes. *CYP3A4* and *CYP3A43* respectively, both of
361 which metabolize anti-TB drug rifampicin were upregulated in Mtb infected HepG2 by
362 approximately 4-fold and 2-fold respectively **(Fig S10A).** Moreover, *NAT2* gene
363 responsible for N-acetylation of isoniazid was also upregulated in the Mtb infected HepG2
364 by almost 2-fold) **(Figure S10 A).** We therefore argued that hepatocyte resident Mtb may
365 display higher tolerance to rifampicin. Towards this, we treated Mtb-infected HepG2 and
366 PHCs with different concentrations of Rifampicin (0.1, 0.5, 5 µg/ml) for 24 hours and CFU
367 enumerated the bacterial after lysis. RAW 264.7 was kept as macrophage control with
368 the similar experimental setup. The percentage of bacteria which survived the drugs was
369 the drug tolerant population. Both HepG2 and PHCs resident Mtb were significantly
370 tolerant to (25-30%) to rifampicin, as compared to the macrophages **(Fig
371 7A and B).** Almost 10 percent of the bacterial population in HepG2 display a tolerogenic
372 phenotype at the highest antibiotic concentration **(Fig 7B).**

373 We also examined Mtb susceptibility to isoniazid (INH), another first line anti-TB drug
374 which is predominantly metabolized (50–90%) via N-acetylation of its hydrazine
375 functionality by arylamine N-acetyltransferase 2 (*NAT2*)[43]. Interestingly, KEGG analysis
376 of transcriptomic data suggested several genes in this pathway to be upregulated in
377 hepatocytes infected with Mtb **(Fig S10 B).** Experimental studies indeed showed higher
378 tolerance of Mtb to INH in both primary hepatocytes and HepG2 at different
379 concentrations (0.1, 0.5, 5 µg/ml) **(Fig 7A and C).** To corroborate the CFU data, we
380 repeated the same experiment **(Fig 7A)** and looked at the bacterial load within each of
381 murine PHCs and BMDMs using high-resolution confocal microscopy. Mouse BMDMs
382 were as a macrophage control. Here also we have calculated the % tolerance as a ratio
383 by measuring the mean fluorescent intensity of GFP-Mtb per hepatocyte treated with drug
384 to MFI of GFP-Mtb per hepatocyte treated with DMSO (control). Extensive analysis of
385 more than 200 cells distinctly showed presence of more Mtb within PHCs treated with

386 both rifampicin and isoniazid than in BMDMs treated with the same concentration of the
387 drugs **(Fig 7D, E and S11A).**

388 To check whether some of these key DMEs are also altered in the Mtb infected mice liver,
389 we did qRT-PCR of some key DMEs related top both rifampicin and isoniazid metabolism.
390 Transcript levels of some of the key DMEs (were upregulated in the liver of the infected
391 mice, 8 weeks post-infection like *Nat2, Cyp2e1, Slco1b2*, *Ces1, Ces2, and*
392 *Aadac* (upregulated by almost 2-3-fold) **(Fig 7F).**

393 Drug tolerance is a bacterial property influenced by both bacterial and host-induced
394 factors. To check whether Mtb derived from hepatocytes, post-drug exposure has altered
395 drug sensitivity or not, we conducted a resazurin microtitre assay with different dilutions
396 of both rifampicin and isoniazid with Mtb derived from PHCs treated with DMSO, Mtb
397 derived from PHCs post-exposure to rifampicin and Mtb derived from PHCs post-
398 exposure to isoniazid. Mtb from all three different setups did not show any alterations in
399 their MIC values, displaying no change in drug sensitivity (**Fig S12 A**). The increased
400 tolerance of Mtb within the hepatocytes can also be attributed to the increased activity of
401 the drug efflux pumps. Drug efflux pumps like Rv1258c, Rv1410, and Rv1819c are known
402 to get upregulated under drug stress conditions, preventing the accumulation of the drugs
403 and thereby decreasing drug sensitivity. To this end, we isolated intracellular Mtb RNA
404 from HepG2 treated with DMSO, 0.5 µg/ml rifampicin, and 0.5 µg/ml isoniazid and
405 checked for the expression of key drug efflux pumps like *Rv 1258c. Rv1410, Rv1819* etc
406 in these three Mtb populations **(Fig S12 B, C and D).** Interestingly, quantitative RT-PCR
407 analyses of these Mtb genes did not show any upregulation of these transporters in Mtb
408 derived from HepG2 exposed to rifampicin and isoniazid, indicating that drug tolerance
409 phenotype can be better attributed to host intrinsic factors rather than Mtb efflux pumps.
410 Our data show that Mtb-infection of hepatocytes induces DMEs, and this host-specific
411 extrinsic activation may result in decreased bioavailability or increased inactivation of anti-
412 TB drugs.

413

414

415 **Discussion**

416 Over the years, various anatomical and cellular environments conducive to Mtb infection
417 have been identified, particularly concerning its latency[44, 45]. Pulmonary TB typically
418 presents with classical symptoms such as persistent coughing and mucus production due
419 to lung involvement[7]. While systemic manifestations like weight loss, fatigue, and loss
420 of appetite are commonly linked to TB progression, the underlying factors driving these
421 metabolic derangements remain unexplored. Our study sheds light on hepatocytes as a
422 previously unrecognized site for Mtb survival and replication, thereby extrapolating the
423 current understanding of TB beyond its pulmonary focus. By combining *in vitro*, *ex vivo*,
424 *in vivo*, and clinical data, we demonstrate that Mtb not only persists within hepatocytes
425 but also induces important metabolic reprogramming, with significant implications for
426 disease progression, symptomatic manifestations, and drug tolerance.

427 A central finding of our work is the Mtb-mediated activation of peroxisome proliferator-
428 activated receptor gamma (PPARγ) in hepatocytes. PPARγ activation leads to the
429 accumulation of cholesterol esters (CE 16:0, 18:0, 18:1), diacylglycerols (DAGs 36:1,
430 36:2, 34:1), and triacylglycerols (TAGs 18:1/36:2, 18:0/36:2, 18:0/36:1). These lipid pools
431 contribute to the formation of lipid droplets, which colocalize with intracellular Mtb, serving
432 as a nutrient reservoir that facilitates bacterial persistence and proliferation. The
433 upregulation of key TAG biosynthesis genes such as *Tgs1*, *Tgs4*, and *Rv1760* in Mtb
434 residing within hepatocytes underscores a transcriptional rewiring within the pathogen to
435 assimilate lipids as a source of their nutrients. Our pharmacological studies using PPARγ
436 agonist and antagonist demonstrated that modulation of PPARγ directly impacts Mtb
437 burden in hepatocytes, confirming the pivotal role of PPARγ in Mtb survival in
438 hepatocytes. The lipid remodeling induced by Mtb infection in hepatocytes is recapitulated
439 in the murine aerosol model, where an increased number of lipid droplets was observed
440 at week 8, accompanied by localized accumulation of immune cells and granuloma-like
441 structures. These findings are consistent with previous reports in macrophages where
442 PPARγ activation enhances lipid biosynthesis, regulates immune responses, and
443 impedes host cell apoptosis[46, 47]. Recent findings have further underscored
444 heightened levels of PPARγ in peripheral blood mononuclear cells (PBMCs) from TB

445 patients with elevated cortisol levels and increased disease severity[48]. However,
446 hepatocytes are uniquely positioned in systemic lipid regulation, engaging in de novo fatty
447 acid synthesis, TAG synthesis, β-oxidation, and lipoprotein metabolism[22, 49]. Mtb-
448 mediated perturbation of these vital processes can lead to a sequela of metabolic
449 disorders such as non-alcoholic fatty liver disease (NAFLD), dyslipidemia and insulin
450 resistance. In macrophages, heightened intracellular lipid levels have been observed to
451 impede autophagy and the acidification of phagolysosomes, both crucial for bacterial
452 eradication[50]. Despite these parallels, comparative transcriptomic analyses of infected
453 HepG2 cells with THP1 cells highlight differences in pathways such as vacuolar and
454 vesicular transport, xenobiotic metabolism, macroautophagy, and cellular respiration.
455 Furthermore, hepatocytes secrete hepatokines, a class of proteins serving as signaling
456 molecules, with diverse roles in metabolism, inflammation, and energy homeostasis,
457 thereby influencing the host-pathogen interplay[13]. Intriguingly, a recent investigation
458 demonstrated that hepatic PPARγ activation induces the expression of growth
459 differentiation factor 15 (GDF-15), a crucial regulator of weight loss observed in ketogenic
460 diets[51].

461 Additionally, we suggest that Mtb infection of hepatocytes creates a drug-tolerant
462 environment in the liver due to activation of DMEs, many of which are earlier shown to
463 metabolize the two frontline drugs, isoniazid and rifampicin. Moreover, lipid accumulation
464 in the liver might also indirectly alter the levels of drug metabolizing enzymes as reported
465 in previous studies[42, 52]. Upregulation of transcripts is not only observed in infected
466 cells *in vitro*, but also in the livers of mice eight weeks after Mtb infection. Particularly
467 noteworthy is the upregulation of NAT-2, which controls the rate-limiting step of
468 acetylating isoniazid into acetylisoniazid. This metabolite is further processed into
469 acetylhydrazine and isonicotinic acid, ultimately reducing the drug's effectiveness against
470 Mtb. Similarly, key rifampicin-metabolizing esterase genes such as Ces1, Ces2, Aadac,
471 and transporter Slco1b2 exhibit upregulation, potentially influencing the drug's distribution
472 and metabolism in the body. The activation of DMEs can significantly modify the
473 pharmacokinetics and pharmacodynamics of anti-TB medications, resulting in suboptimal
474 drug concentrations and the emergence of drug-resistant strains[53].

475 Pulmonary tuberculosis (TB) can lead to miliary through hematogenous dissemination,
476 where Mtb spreads from the infected lungs into blood vessels either from a primary lung
477 focus, reactivated TB or caseous necrosis. Once in blood vessels, the bacteria seed
478 multiple organs, forming tiny granulomas, characteristic of miliary TB. The liver becomes
479 involved either through direct hematogenous spread or extension from nearby infected
480 lymph nodes, leading to hepatic TB, which presents with granulomas and liver
481 dysfunction. This systemic spread underscore the severity of untreated pulmonary TB
482 and the need for early intervention[54-57]. Our murine and guinea pig aerosol infection
483 models demonstrated progressive liver involvement starting at week 4, with the presence
484 of lipid-laden hepatocytes, localized immune infiltrates, and granuloma-like structures.
485 Importantly, liver biopsy samples from TB patients revealed ectopic granulomas and Mtb
486 antigen (Ag85B) localization within hepatocytes, highlighting the clinical relevance of our
487 findings. While previous research has explored liver infection by Bacillus Calmette-Guérin
488 (BCG) using an intra-venous model in mice, the bacilli were predominantly found within
489 tissue-resident macrophages or Kupffer cells at 15 minutes and 2 days post-infection[58].
490 However, our study consistently identified the presence of Mtb within hepatocytes in a
491 murine aerosol infection model after the fourth week. Similarly, in a guinea pig aerosol
492 infection model, liver infection was evident, marked by distinct granulomas by week 4.
493 Furthermore, analysis of human biopsy liver samples from pulmonary TB patients
494 revealed ectopic granuloma-like structures within the liver hepatocytes, with the presence
495 of Mtb-specific Ag85B signals within hepatocytes. Together, these findings underscore
496 hepatocytes as a novel niche for Mtb persistence, shedding new light on the pathogenesis
497 of TB. Interestingly, in infected armadillos, *M. leprae* is shown to infect hepatocytes and
498 hijack liver homeostatic, regeneration pathways to promote *de novo* organogenesis[59].

499 Although animal models offer valuable insights into Mtb infection and TB pathology, they
500 fall short of fully replicating the complexities of human TB. Several recent studies in
501 COVID-19 patients have shown that hepatocytes get infected with SARs-CoV-2, thereby
502 increasing gluconeogenesis and hyperglycemia[60, 61]. With compelling reports
503 associating hepatic steatosis with the onset of type 2 diabetes mellitus (T2DM), we
504 speculate that TB-induced perturbations in lipid metabolism might predispose chronic TB
505 patients to T2DM and vice versa[62, 63]. Through our investigation, we propose that

506 future studies in human TB patients might scrutinize this metabolically rich hepatocyte
507 niche to understand multiple organ-wide derangements in TB pathogenesis.

508 **Materials and Methods**

509 **Ethical clearances**

510 **Human studies:**

511 Paraffinized non-Mtb infected, and Mtb-infected human autopsied liver specimens were
512 obtained from the Postgraduate Institute of Medical Education and Research,
513 Chandigarh, India. The Institutional Ethics Committee of CSIR-IMTech (Council of
514 Scientific and Industrial Research-Institute of Microbial Technology) approved all research
515 experiments involving human samples (Approval no [IEC (May 2021) #6]). The samples
516 utilized in the study are from a library of autopsied human specimens in PGIMER
517 (Postgraduate Institute of Medical Education and Research). The consent is provided by
518 the relatives of the deceased person while its submission to the PGIMER.

519 **Animal studies:**

520 All the mice (C57BL/6) were housed in the animal house at the National Institute of
521 Immunology (NII) before being transported to the TACF-ICGEB (Tuberculosis Aerosol
522 Challenge Facility), for subsequent animal infection studies. The animal experiments
523 were performed adhering to the institutional guidelines (Approval number: Institutional
524 Animal Ethical Committee, IAEC 543/20.). Female Hartley Dunkan guinea pigs were used
525 for infection studies in TACF-ICGEB in accordance with the institutional guidelines
526 (Approval number: Institutional Animal Ethical Committee, IEAC #440/17)

527 **Confocal microscopy and Immunofluorescence measurements:**

528 Lipid droplets were stained by BODIPY 493/503 dye. Primary mouse hepatocytes and
529 HepG2 cells were grown on 12 mm coverslips at respective densities as per the
530 experimental requirement. Cells were washed with 1X PBS (HiMedia M1452-500G), fixed
531 by 4% paraformaldehyde, and incubated at room temperature for 15 minutes. After
532 incubation, the cells were washed thrice with 1X PBS followed by staining with 10 μM
533 BODIPY dye in 1XPBS for 45 minutes at room temperature. After the staining, the excess

534 dye was removed by washing thrice with 1X PBS. To check for the acidified compartments
535 within the cells, LysoTracker Red DND-99 (L7528) was added to the cells at a
536 concentration of 500 nM for 30 minutes at 37° Celsius, followed by washing thrice with
537 1X PBS to remove the residual dye. The cells were fixed with 4% paraformaldehyde as
538 previously mentioned. For staining with various antibodies, the cells were permeabilized
539 with 0.2% Triton-x 100 (X-100-1L) for 15 minutes, followed by proper washing with 1X
540 PBS. The cells were then blocked by 2% BSA in 1X PBST for 1 hour at room temperature.
541 Post blocking, the cells were treated with primary antibody overnight at 4°Celsius,
542 followed by proper washing with 1X PBS. Secondary antibody (1:500 dilution) was added
543 to the cells for 1 hour at room temperature. Three washes with 1X PBS were given. The
544 nucleus was stained with DAPI (Sigma D9542-5MG) at 1ug/ml concentration for 20
545 minutes at room temperature. The excess DAPI was washed with 1X PBS followed by
546 mounting with ProLong Gold Antifade mountant (P36930). Images were acquired by Zeiss
547 LSM 980 Laser scanning confocal microscope.

548

549 **Image Analysis:**

550 Analysis was done using Image J and Zen blue software. Mean fluorescent intensity/ cell
551 was calculated by corrected total cell fluorescence (CTCF) = Integrated Density – (Area
552 of Selected Cell x Mean Fluorescence of Background readings). Signal intensity in tissue
553 sections were normalized to respective areas. For colocalization of Mtb with various intra-
554 cellular markers, each data point represents a single field with 6-8 infected cells. More
555 than 100 cells across 4 independent experiments were analyzed. Serial confocal sections
556 were acquired with Z-stacks spanning 10-15 uM. The percentage of Mtb in the respective
557 markers were calculated by calculating the Mtb voxels colocalizing in the respective
558 markers. The image was analyzed by Zen Blue software (Zeiss) and Image J.

559 For percentage tolerance of Mtb within hepatocytes, we have calculated the ratio by
560 measuring the mean fluorescent intensity of GFP-Mtb per hepatocyte treated with drug
561 to MFI of GFP-Mtb per hepatocyte treated with DMSO (control). BMDMs were used as
562 the macrophage control. More than 20 fields, each consisting of more than 4 infected

563 cells have been used for analysis. MFI/ cell was calculated using the Zeiss ZEN blue
564 image analysis software

565 **Tissue Immunofluorescence staining:**

566 **Paraffin sections**

567 Five-micron thick sections of paraffin-embedded tissue sections were taken in poly-L-
568 Lysine coated slides (P0425-72EA). Deparaffinization was performed by heating the
569 slides at 50°C for 20 seconds (3 times) till the wax melts, followed by the subsequent
570 steps, 100% xylene (Merck, CAS-1330-20-7) for 10 minutes (3 times), xylene and
571 absolute ethanol (Merck, CAS- 64-17-5) for 10 minutes, 100% ethanol for 10 minutes,
572 70% percent ethanol for 5 minutes (2 times), 50% ethanol, distilled water for 5 minutes
573 (2minutes) and a final wash in 1x PBS for 5 minutes (2 times). Antigen retrieval was
574 performed in an antigen retrieval buffer (10mM Sodium Citrate, 0.05% tween-20, pH: 6)
575 by heating the slides at 60°C for 15 minutes. After antigen retrieval, permeabilization was
576 performed with 0.4% Triton-X 100 in 1X PBS for 20 minutes followed by proper washing
577 with 1x PBS. Blocking was done with 5% BSA for 1 hour. Sequential addition of primary
578 antibody was performed at 1:100 dilution at 4°C overnight. Primary antibody was washed
579 with 1X PBS followed by counter stain with DAPI nuclear stain at 1 ug/ml concentration.
580 Mounting was done with a drop of vectashield (sigma-aldrich, F6182-20ml). The slides
581 were visualised in Zeis LSM 980 confocal microscopy at 40X (oil) magnification.

582 **Cryosections**

583 Seven-micron thick cryosections were taken in poly-L-Lysine coated slides (P0425-
584 72EA). The sections were washed with 1X PBS, 3 times for 5 mins each. Permeabilisation
585 was done with 0.25% Triton-X 100 in 1X PBS for 15 minutes followed by washing with 1X
586 PBS. Blocking was done with 5% BSA for 1 hour followed by incubation with primary
587 antibody overnight at 4°C. After that the slides were washed with 1X PBS 2 times for 5
588 minutes each followed by incubation with fluorophore conjugated secondary antibody for
589 45 minutes. The slides were washed with 1X PBS followed by counterstain with DAPI at
590 1ug/ml concentration. Mounting was done with a drop of Vectashield (Sigma-Aldrich,

591 F6182-20ml). The dilution of the dyes and antibodies used in the staining are mentioned
592 in the table.

593 For staining with BODIPY, the sections were incubated with 15 ums of BODIPY for 40
594 minutes at room temperature. The slides were visualized in Zeis LSM 980 confocal
595 microscopy at 40X (oil) magnification.

596 **Fluorescence in-situ hybridization:**

597 FISH was used to detect Mtb in infected human liver following published protocols (1-3).
598 Briefly, the paraffinized human liver tissue sections were initially deparaffinized using a
599 serial washing step with xylene and ethanol, following which the sections were treated
600 with 1 mg/ml Proteinase K and 10 mg/ml Lysozyme in 10 mM Tris (pH 7.5) at 37°C for 30
601 min. Next, the samples were incubated in the Prehybridization buffer at 37°C for 1 h.
602 Prehybridization buffer is composed of 20% 2X Saline sodium citrate (SSC), 20% Dextran
603 sulfate, 30% Formamide, 1% 50X Denhardt's reagent, 2.5% of 10 mg/ml PolyA, 2.5% of
604 10 mg/ml salmon sperm DNA, 2.5% of 10 mg/ml tRNA. The slides were thoroughly
605 washed with a 2X SSC buffer. The sections were then incubated in hybridization buffer at
606 95°C for 10 min and then chilled on ice for 10 min. Further hybridization was allowed at
607 37°C overnight. Hybridization buffer is composed of prehybridization buffer plus 16S Mtb-
608 H_{37} Rv probe (5′ FITC – CCACACCGCTAAAG – 3′), which is specific for the 16S rRNA
609 of Mtb at a final concentration of 1 ng/µl. The liver tissue sections were next subjected to
610 a series of washing steps with 1X SSC at room temperature for 1 min, 1X SSC at 55°C
611 for 15 min, 1X SSC at 55°C for 15 min, 0.5X SSC at 55°C for 15 min, 0.5X SSC at 55°C
612 for 15 min, 0.5X SSC at room temperature for 10 min. Coverslips were mounted on glass
613 slides and visualized using Nikon A1R confocal microscope with a 488 nm laser.

614 **Acid Fast Staining and Auramine O and Rhodamine B staining in liver sections.**

615 Acid-fast staining was performed using a ZN Acid Fast Stains-Kit (K005L-1KT, HIMEDIA).
616 Prior to staining, the paraffinized samples were deparaffinized using a serial washing step
617 with xylene and ethanol 1. 100% Xylene for 6 min, 2. Xylene: Ethanol 1:1 for 3 min, 3.
618 100% Ethanol for 3 min, 4. 95% Ethanol for 3 min, 5. 70% Ethanol for 3 min, 6. 50%
619 Ethanol for 3 min, 7. Distilled water. The glass slides were flooded with Carbol Fuchsin

620 stain and heated to steam for 5 min with a low flame. The glass slides were allowed to
621 stand for 5 min without further heating. The glass slides were then washed in running tap
622 water. The glass slides were decolorized with acid-fast decolourizer for 2 min. 5. Washed
623 with tap water. 6. Counterstain for 30 sec with Methylene Blue Washed with tap water,
624 dried in air, and examined under 100x objective with oil immersion. The presence or
625 absence of bacteria in infected and uninfected samples was checked through staining
626 with Phenolic Auramine O-Rhodamine B dye (4) (1/3 dilution of stock solution) (Auramine
627 O-861020-25gm, Sigma) (Rhodamine B-R6626-100gm, Sigma). Coverslips were
628 mounted on glass slides and visualized using CLSM with a 488 nm laser.

629 **Bacterial cultures and in-vitro experiments:**

630 Virulent laboratory strains of H37Rv, BCG, and GFP-H37Rv bacterial cultures were
631 cultivated on 7H9 medium (BD Difco) supplemented with 10% Oleic Acid-Albumin-
632 Dextrose-Catalase (OADC, BD, Difco),0.05% glycerol and 0.05% tween 80 under shaking
633 at 37°C conditions for in vitro assays. The cultures were then incubated in an orbital
634 shaker at 100 rpm and 37 °C until the mid-log phase. pMN437-GFPm2 vector (Addgene,
635 32362) was used to electroporate the virulent H37Rv strain to create GFP-H37Rv, which
636 was then maintained in 50 µg/ml hygromycin 7H9-OADC medium. pMSP12: mCherry
637 plasmid (Addgene No. 30169) was electroporated in H37RV to generate Mtb-H37Rv-
638 mCherry.To prepare the single-cell suspension needed for infection tests, bacterial
639 cultures were passed through a sequence of different gauge needles five times through
640 23-gauge, 26-gauge, and three times through 30-gauge.

641 Human monocytic cell line THP-1 were obtained from American Type Culture Collection
642 (ATCC) and cultured in RPMI-1640 medium with 10% FBS at 37 °C and 5% CO2
643 incubator. THP-1 derived macrophages were obtained by incubating THP-1 cells with 20
644 ng/ml phorbol 12-myristate 13-acetate (PMA, sigma) for 24 hours followed by washing
645 and maintenance in complete media. The cells were kept in non-PMA containing
646 complete media for 16-20 hours before infection with Mtb. HepG2, Huh-7, RAW 264.7
647 and PHCS were grown in DMEM under with 10% FBS at 37 °C and 5% CO2 incubator.

648 AML-12 cells were cultured in DMEM media containing 1X insulin-transferrin-selenium
649 supplement (ITS-G), under the above-mentioned conditions.

650 In-vitro and ex-vivo infection experiments in primary cells and different cell lines were
651 performed at a Multiplicity of infection of 10 (MOI: 10) for both CFU enumeration and
652 confocal microscopy. The macrophage experiments involving THP-1 and RAW 264.7
653 involved incubating the cells with Mtb-H37Rv for 5-6 hours followed by washing with 1X
654 PBS and amikacin treatment (200 ug/ ml for 2 hours) to remove the extracellular bacteria.
655 The cells were kept for the designated time points for 24 hours, 48 hours and so on and
656 then lysed with lysis buffer (0.05 % SDS in 1X PBS) followed by plating in 7H11 plates.

657 For primary mouse hepatocytes and AML-12 cells, the cells were infected with the Mtb at
658 a multiplicity of 10 for 8 hours followed by amikacin treatment (200 ug/ ml for 2 hours).
659 For HepG2 and Huh-7, the time of incubation was 5- 6 hours followed by washing with
660 1X PBS and amikacin treatment as previously mentioned to remove the extracellular
661 bacteria.

662 The percentage drug tolerant population was calculated using the following formula (A/B
663 X 100) where A is the CFU in the drug treated group, B is the CFU in the untreated group.
664 The cells were morphologically checked for signs of cell death before proceeding with the
665 plating. For the inhibitor and inducer experiments, the cells were treated with the
666 respective drugs for 48 hours post uptake of Mtb. After that they were lysed and Mtb CFU
667 was enumerated.

668 **Standardization of Multiplicity of infection (MOI) for PHCs and HepG2:**

669 To standardise the MOI, HepG2 and BMDMs were infected with the following MOI of GFP-
670 Mtb as per the standardized protocol: 1, 2.5, 5 and 10. 6 hours post-infection, the cells
671 were trypsinised and fixed with 2% PFA. The percentage uptake was calculated by flow
672 cytometry. For, PHCs, the cells were infected at the above-mentioned MOI and
673 percentage infection was calculated by microscopy as (# of cells with GFP-Mtb/Total # of
674 cells *100)

675 **C57BL/6 aerosol challenge:**

676 The mice infection experiments were conducted in the Tuberculosis Aerosol Challenge
677 Facility (TACF, ICGEB, New Delhi, India). C57BL/6 mice were placed in individual
678 ventilated cages within the enclosure, maintaining a temperature of 20-25ºC, 30-60 %

679 humidity and 12h-12h of light-dark cycle. Following the standardized protocol, mice were
680 infected with 200 CFUs of H37Rv in a Wisconsin-Madison chamber. To ensure proper
681 establishment of infection, two animals were euthanized 24 hours post aerosol challenge.
682 The lungs were harvested and homogenised in 1X PBS and plated in Middlebrook 7H11
683 agar plates (Difco) supplemented with 10% OADC and 0.5% glycerol. CFU enumeration
684 was done three weeks post plating.

685 **C57BL/6 peritoneal infection:**

686 The mice were injected with 10^6 CFUs of H37Rv in 0.2 ml of 1X PBS. Following infection,
687 on different days post infection, the lung, spleen, and the liver was harvested and
688 homogenized and plated in Middlebrook 7H11 agar plates (Difco) supplemented with 10%
689 OADC and 0.5% glycerol. CFU enumeration was done three weeks post plating.

690

691

692

693 **List of antibodies and dyes used in the study:**

Serial number	Antibodies and dyes	Catalogue number	Company	Application and dilution
1.	Rab5	2143T	CST	IF/ICC (1:200)
2.	Rab7	D9F2	CST	IF/ICC (1:200)
3.	Cathepsin D	Ab75852	Abcam	IF/ICC (1:150)
4.	LAMP1	9091T	CST	IF/ICC (1:200)
5.	EEA1	3288T	CST	IF/ICC (1:200)
6.	ASPGR1	PA5-32030	Invitrogen	IF/ICC (1:500)
7.	PPAR γ	PA3-831A	Invitrogen	IF/ICC (1:150)

				WB (1:1000)
5.	Ag85B	Ab43019	Abcam	IF/ICC (1:800)
6	CD45-APC (clone 104)	558702	BD biosciences	1:300
7.	β-actin rabbit polyclonal Antibody.	4967	CST	IF/ICC (1:100) WB (1:2000)
8.	Goat anti-rabbit IgG (H+L) secondary Ab Alexa fluor 555 Plus	A32732	Thermo fischer Scientific	IF/ICC (1:400)
9.	Goat anti-rabbit IgG (H+L) Secondary Antibody, Alexa Fluor 488	A11008	Thermo fischer Scientific	IF/ICC (1:400)
10.	Goat anti-rabbit IgG (H+L) Secondary Antibody, Alexa Fluor 405	A-31556	Thermo fischer Scientific	IF/ICC (1:400)
11.	Lysotracker Red	L7528	Invitrogen	500 nM
12.	BODIPY-493/503	D3922	Invitrogen	Staining (10-15 μM)
13.	BODIPY 558/568 C12	D3835	Invitrogen	Metabolic Labelling (7.5 μg/ml)

14.	Phalloidin-Alexa fluor 488	A12379	Invitrogen	IF/ICC 1 unit/slide
15.	Phalloidin-Alexa Fluor 555 plus	A30106	Invitrogen	IF/ICC 1 unit/slide
16.	HCS LipidTOX Red Neutral Lipid Stain	H34476	Invitrogen	IF/ICC (1:400)
17.	DAPI	D9542	Sigma-aldrich	1 ug/ml
18.	ZN Acid Fast Stains	K005L-1KT	Himedia	
19.	Auramine O	861020-25gm	Sigma-Aldrich	
19	Rhodamine B	R6626-100gm	Sigma-Aldrich	

694

695

696 **List of reagents in the study:**

Serial no	Reagents	Catalogue number
1.	C75	C5490-5MG, Sigma-Aldrich
2.	OA-BSA	O3008-5ML, Sigma-Aldrich
5.	GW9662	M6191-25MG, Sigma-Aldrich
6.	Rosiglitazone	R2408-10MG, Sigma-Aldrich
7.	T863	SML0539-5MG, Sigma-Aldrich
8.	Rifampicin	557303-1G, Merck

9.	Isoniazid	I3377-5G, Merck
10.	PMA (Phorbol 12-myristate 13-acetate)	P8139-1MG, Merck
11.	Mouse MCSF (macrophage colony stimulating factor)	130-101-706 (25 µg), Miltenyi Biotec
12.	Insulin-Transferrin-Selenium (ITS - G) (100X)	41400045, Gibco

697

698 **Sorting of labelled H37Rv cells**

699 The infected hepatocytes were trypsined and washed with 1X PBS followed by passing
700 through 40µm cell strainer to make single cell suspension. After that the cells positive for
701 mCherry signals were sorted using the BD FACS Aria at TACF, ICGEB. Approximately 1
702 million cells were used for RNA isolation per sample.

703 **Primary hepatocyte Isolation:**

704 After euthanizing the mice, the peritoneal cavity was opened, and the liver was perfused
705 with 1X HBSS solution till exsanguination was complete. After that collagenase solution
706 (17 mg in 30 ml of 1X HBSS) was passed for digestion. The liver was cut into small pieces
707 and kept in 25 ml of DMEM media followed by lysing the tissues with a glass pestle and
708 sieve. The cells were then passed through a 70 µM cell strainer. 25 ml of Percoll was
709 added to the cells with proper mixing. It was centrifuged at 1000 rpm for 5 minutes. The
710 floating cells were removed, and a brownish layer of pure hepatocytes pelted at the
711 bottom. The cells were counted and plated according to the experimental need on a
712 collagen coated plate.

713 **Isolation of Bone marrow derived macrophages (BMDMs) from mouse:** BMDMs
714 used for Mtb infection studies were isolated following the published protocol with minor
715 modifications[64]. Briefly, the epiphysis of the femurs and tibia from C57BL/6 mice were

716 cut and the bone marrow were gently flushed into BMDM supplemented with 10% FBS
717 and 1% penicillin streptomycin. The bone marrow cells were centrifuged at 200 X g for 5
718 minutes at 4° C. The cell pellet was aspirated with 1X PBS and treated with RBC Lysis
719 buffer (for 3 minutes on ice, followed by the addition of complete media. The cells were
720 resuspended in 5 ml of the media and passed through a 70 µm cell strainer. The cells
721 were seeded in complete DMEM supplemented with 10ng/ml of MCSF. On the third day,
722 half of the media volume was replaced by fresh DMEM supplemented with 10ng/ml of
723 MCSF. On the 7th day, the cells were trypsinised, counted and seeded according to
724 experimental requirements.

725 **Lipid Extraction protocol and Mass spectrometry:**

726 5 million HepG2 cells were infected with Mtb-H37Rv at MOI 10 and kept for 24 hours and
727 48 hours post-infection. An equal number of uninfected cells were taken. The cells were
728 scrapped, and the procedure of Bligh and Dyer was followed[65]. In brief, the cells were
729 lysed in 1% Triton X-100 after being rinsed twice with 1X PBS. Following lysis, the lysate
730 was vortexed and four volumes of methanol-chloroform (2:1) were added. After that, one
731 volume each of water, chloroform, and 50 mM citric acid was added and vortexed.
732 Following a 10-minute centrifugation at 10,000 rpm at 4° Celsius, the lower organic phase
733 was collected and dried using liquid nitrogen. All semi-quantitative lipid measurements
734 were done using previously reported high-resolution MS/MS methods and
735 chromatographic techniques on an Agilent 6545 QTOF instrument. All sterols were
736 resolved using a Gemini 5U C-18 column (Phenomenex) while DAGs/TAGs were
737 resolved using a Luna 5U C-5 column (Phenomenex) using established solvent systems.

738 **Cell lysate preparation and Western blotting:**

739 The cells were washed twice with 1X PBS followed by lysis with SDS-RIPA buffer (50 mM
740 Tris-HCl pH 7.5, 150 mM NaCl, 1 mM EDTA, 0.1% SDS, 1% Triton-X 100, 1 mM DTT, 1X
741 Proteinase inhibitor). The cells were incubated with the buffer for 30 minutes in ice
742 followed by vortexing for 5 minutes. The supernantant fraction was collected by
743 centrifuging at 10000 rpm for 20 minutes at 4°C. The protein concentration was
744 determined by bicinchoninic acid (BCA) protein estimation kit (Thermo Fisher Scientific,
745 Waltham, Massachusetts, USA, 23227) following the manufacturer's protocol. 60-80 ug

746 of protein was resolved in SDS-PAGE followed by transferring onto a PVDF membrane.
747 Blocking was done in 5% skimmed milk in 1X TBST followed by incubation with primary
748 antibodies overnight at 4°C. The membranes were washed 3 times with 1x TBST for 10
749 minutes each followed by incubation with the HRP-conjugated secondary antibody for 1
750 hour. Immobilon HRP substrate was used to develop the blots and ImageQuant
751 Chemiluminescent imaging system (LAS 500) was used to acquire the images. Band
752 intensities were measured by using ImageJ.

753 **MIC determination of Mtb isolated from primary hepatocytes and primary**
754 **hepatocytes treated with Rifampicin and isoniazid:**

755 Mtb was isolated from primary hepatocytes, primary hepatocytes treated with 0.5µg/ml of
756 rifampicin and primary hepatocytes treated with 0.5µg/ml of isoniazid. These bacteria
757 were grown to a logarithmic phase of OD_{600}= 0.6 in Middlebrook 7H9 broth supplemented
758 with 10% OADC, 0.05% glycerol and 0.05% tween 80 under shaking conditions. Single-
759 cell suspension of the Mtb was made as previously described. Two-fold serial dilutions of
760 both rifampicin and isoniazid was prepared in 0.1 ml 7H9-OADC (without Tween 80) (The
761 concentration and the dilution of the drugs have been mentioned in the figure) in 96-well
762 flat bottom microplates. Approximately $5X10^4$ Mtb cells were added to each well in a
763 volume of 0.1 ml. Control wells containing (Mtb only, medium+ inhibitor and only medium)
764 were included in the plate setup. The plate was incubated at 37°C 5 days, followed by the
765 addition of 20 µl of 0.02% resazurin for 24 hours. Visually, minimum inhibitory
766 concentration (MIC) was noted as the lowest drug concentration that prevented the
767 change of colour from blue to pink.

768 **qRT-PCR of intracellular Mtb isolated from hepatocytes:**

769 HepG2 cells were infected with Mtb at a MOI of 10 and at the respective time points post-
770 infection, the intracellular Mtb was isolated. In all experiments, the cells were treated with
771 amikacin to remove the extracellular bacteria, followed by subsequent washing by 1X
772 PBS. 4M Guanidine isocyanate was added to the flasks in equal amount to the media
773 and the cells were scrapped. The suspension was centrifuged at 3500 rpm for 7 minutes
774 and the pellet was resuspended in 350 µl of the RNA Lysis buffer of MN Kit (740955.250),
775 followed by beat beating. RNA was isolated as per the manufacturer's protocol. Isolated

776 RNA was treated with Dnase (PGM052, Puregene) for 1 hour to remove genomic DNA
777 contamination. RNA integrity was checked by running it on a 2% agarose gel with RNA
778 loading dye.

779 1 µg of RNA was reverse transcribed to cDNA using the Takara cDNA synthesis kit
780 (6110A) as per the manufacturer's protocol. Gene expression analysis by quantitative
781 real-time PCR was performed PowerUp SYBR Green PCR (Thermo fischer scientific,
782 (A25742) master mix in ABI 7500 FAST instrument. 16S rRNA was used as the
783 normalizing control and comparative Ct method was used for quantification.

784 **Fluorescent fatty acid labelling of HepG2 and isolation:**

785 HepG2 cells were incubated with 7.5 µg/ml of fluorescently tagged fatty acid (BODIPY
786 558/568 C_{12}) for 24 hours. The unincorporated fatty acids were removed by washing it
787 with 1X PBS, three times. After that the cells were treated with DMSO or inhibitors (T863
788 and C75) for 24 hours, followed by infection with Mtb at a MOI of 10, following the
789 standardized protocol of infection. A separate set of cells before infection were analysed
790 for the effect of the inhibitors on LD formation by microscopy.

791 After, 48 hours post infection, the cells were washed with 1X PBS and treated with Triton
792 X -100 (0.05% v/v in water), probe sonicated, and Mtb from the cells were isolated by
793 centrifuging at 3500 RPM for 8 minutes. Isolated Mtb cells were washed with 1X PBS and
794 fixed with 4% PFA and stained with DAPI (1mg/ml). The cells were mounted on poly-L-
795 lysine coated slides with antifade agent. The cells were visualised in Zeiss 980 LSM
796 confocal microscope at 100X, magnification.

797 **Gene expression studies**

798 **RNA isolation**

799 Total RNA was isolated from HepG2, PHCs and liver sections using the MN-NucleoSpin
800 RNA isolation kit (740955.250) following the manufacturer's protocol. For RNA
801 sequencing, an equal number of cells was used during isolation. For Liver tissue,
802 approximately 10mg was tissue was used. The quality of the RNA was verified by running
803 it on a 1.5% agarose gel and by monitoring 260/280 ratios. All the RNA samples were

804 frozen together in -80ºC. For RNA sequencing, 3-5 ug of RNA was shipped in sodium
805 acetate buffer (3 M Sodium acetate, pH 5.2) with 100% Ethanol. 4 biological replicates
806 from each time point were sent for sequencing. The RNA samples with RNA integrity
807 number (RIN > 8.5) were used for library preparation.

808

809 RNA samples (for four biological replicates) were subjected to pair-end RNA sequencing
810 after rRNA depletion on the Illumina platform Novaseq-6000 at CCMB, Hyderabad, India.
811 Quality control and sequence trimming was performed using fastp (v0.23.2). The trimmed
812 paired-end reads were aligned to the human genome (GRCh38) using the HISAT2
813 (v2.2.1) pipeline. Reads were assembled into transcripts using StringTie (v2.2.1).
814 Annotation was conducted using aligned sequences and a GTF annotation file. The
815 mapped reads were then used for generating the count table using StringTie
816 (v2.2.1), genes lacking an Ensembl ID annotation were excluded. We arrived at a list of
817 62694 genes which were used for further analysis (available through GEO accession-
818 GSE256184). The differential count was performed by DEseq2 (R package) using the
819 uninfected samples of respective time points. Pathway enrichment was performed using
820 the GO database and clusters were visualized using the R package ClusterProfiler.
821 Further pathways of interest were analysed by GAGE and visualized using Pathview in
822 KEGG view.

823

824 **cDNA synthesis and RT-qPCR**

825 1ug of RNA was reverse transcribed to cDNA using the Takara cDNA synthesis kit (6110A)
826 as per the manufacturer's protocol. Gene expression analysis by quantitative real-time
827 PCR was performed PowerUp SYBR Green PCR (Thermo fischer scientific, (A25742)
828 master mix in ABI 7500 FAST instrument. Beta-actin was used as the normalizing control
829 and comparative Ct method was used for quantification.

830 **List of primers used in the study**

831

GENE NAMES	FORWARD PRIMER (5'----------->3')	REVERSE PRIMER (5'----------->3')	
β-actin	ATGGAGGGGAATACAGCCC	TTCTTTGCAGCTCCTTCGTT	Mouse
ppar-γ	CTCTGGGAGATTCTCCTGTTGA	GGTGGGCCAGAATGGCATCT	Mouse
ppar-α	AGAGCCCCATCTGTCCTCTC	ACTGGTAGTCTGCAAAACCAAA	Mouse
fasn	CTGCGTGGCTATGATTATGG	AGGTTGCTGTCGTCTGTAGT	Mouse
acat1	CAGGAAGTAAGATGCCTGGAAC	TTCACCCCCTTGGATGACATT	Mouse
acat2	CCCGTGGTCATCGTCTCAG	GGACAGGGCACCATTGAAGG	Mouse
dgat1	TGCCCTGACAGAGCAGATGG	CAGGTTGACATCCCGGTAGG	Mouse
dgat2	TGGCGCTACTTCCGAGACTAC	TGCTGACTTCAGTAGCCTCTGTG	Mouse
nat2	ACACTCCAGCCAATAAGTACAGC	GGTAGGAACGTCCAAACCCA	Mouse
Slco1b2	GGGAACATGCTTCGTGGGATA	GGAGTTATGCGGACACTTCTC	Mouse
aadac	TACCGCTTCCAGATGCTATTGA	ACTGATTCCCAAAAGTTCACCAA	Mouse
cyp2e1	CATCACCGTTGCCTTGCTTG	GGGGCAGGTTCCAACTTCT	Mouse
ces1c	GCACTACGCTGGGTCCAAGAT	AAAGATGGTCACGGAATCCG	Mouse
ces2c	GCTGAATGCTGGGTTCTTCG	GCTGCCTTGGATCTGTCCTGT	Mouse
β-actin	AAGGCCAACCGCGAGAAGAT	GCCAGAGGCGTACAGGGATA	Human
pparγ	GGTGAAACTCTGGGAGATTCT	CTCTGTGTCAACCATGGTCA	Human
fasn	AGTACACACCCAAGGCCAAG	GTGGATGATGCTGATGATGG	Human
acat1	TACCAGAAGTAAAGCAGCATGG	TCATTCAGTGTACTGGCATTGG	Human
acat2	CTTTAGCACGGATAGTTTCCTGG	GCTGCAAAGGCTTCATTGATTTC	Human
dgat1	CAATCTGACCTACCGCGATCT	TCGATGATGCGTGAGTAGTCC	Human

dgat2	GAATGGGAGTGGCAATGCTAT	CCTCGAAGATCACCTGCTTGT	Human
nat2	CCAGAAGGGGTTTACTGTTTGG	CAGGTTTGGGCACGAGATTTC	Human
mgat1	CGCAAGTTCCAGGGCTACTAC	CTTCAGCAGCGGATAGGTGG	Human
fsp27	ATGGACTACGCCATGAAGTCT	CGGTGCTAACACGACAGGG	Human
Rv1258c	CTACGAGGCGATCCTCAACC	CGAGGATGGACAACCCGAAT	Mtb
Rv1819c	ATCGGGGTTTTCAGCGTGAT	GTCGAGCCAGTCTTGTGTGA	Mtb
Rv1218c	ATCGAGATTCGCGGACTGAC	ACATCGCCTGGAACATAGGC	Mtb
Rv1410c	ATGGTGACGCTGGTTGATGT	CGGTAGGGCGATAAGGAACC	Mtb
tgs1 (Rv3130c)	CCTTCTTATCGTCGCTCGCT	GCCAAGATCGAAGTCGGGAT	Mtb
tgs4 (Rv3088)	ACGGTCTCGTTCCTCAACAC	CCGGTGAATCGGAGAGGAAG	Mtb
lipY (Rv3097c)	TCTGCGCTCGAAACTCACTT	GCTCATCCCGTCATAGGTGG	Mtb
acrA1 (Rv3391)	ATGGCGGTCAACTACTTCGG	CCTTGGTGGGCAGATACGAG	Mtb

List of reagents in the study

Reagent	**Company**	**Catalogue number**
Immobilon Forte Western HRP substrate	Millipore	WBLUF0500

Amersham Hybond Western blotting membranes, PVDF	Merck	GE10600023
PowerUP SYBR	Thermo Fischer Scientific	A25742
Vectashield	Sigma-Aldrich	F6182
Primescript 1st strand cDNA synthesis kit	Takara Bio	6110A
NucleoSpin RNA isolation Kit	Macherey-Nagel	74106
ProLong Gold antifade reagent	Thermo Fischer Scientific	P36930
PolyFreeze Tissue Freezing medium	Sigma- Aldrich	SHH0026
Microscope slides	Himedia	BG005
Poly-Prep slides	Sigma- Aldrich	P0425-72EA
2X RNA loading dye	Thermo Scientific	R0641

837 **Softwares**

838 All the graphs have been generated using GraphPad Prism 10 and Microsoft Excel. The
839 schematics have been drawn with the help of Biorender.com.

840 **Acknowledgements**

841 We thank Dr. Lakshyaveer Singh, Tuberculosis Aerosol Challenge Facility (TACF), ICGEB
842 for mice experiments. We thank Dr. Neerja Wadhwa for helping in the NII Central Confocal
843 facility, Mr. Birendra Nath Roy for the preparation of the Cryosections, and the NII animal

facility for providing us with the animals. We thank the Next Generation Sequencing (NGS) facility at CSIR-CCMB for transcriptomic support.

Author Contribution

BS and RSG conceptualized the study and analysed the data. BS, DSG, JS, MY, PS, RDS performed the experiments. Human liver sections were stained by SS under the guidance from AK. Transcriptomic analysis was done by JS. Sorting was done by PS and RDS under the guidance from DK. Mass spectrometry analysis was conducted by AC under the supervision of SSK.KM conducted the guinea pig infection experiments. BS and RSG wrote the manuscript. BS, DM, DSG, AK, SSK, DK and RSG reviewed and edited the manuscript. RSG supervised the project.

Declaration of Interests: The authors declare no conflicts of interests

References:

1. *Global Tuberculosis Report* 2023, World health Organisation (WHO).
2. Seung, K.J., S. Keshavjee, and M.L. Rich, *Multidrug-Resistant Tuberculosis and Extensively Drug-Resistant Tuberculosis*. Cold Spring Harb Perspect Med, 2015. **5**(9): p. a017863.
3. Husain, A.A., et al., *Current perspective in tuberculosis vaccine development for high TB endemic regions*. Tuberculosis (Edinb), 2016. **98**: p. 149-58.
4. Eckhardt, M., et al., *A systems approach to infectious disease*. Nat Rev Genet, 2020. **21**(6): p. 339-354.
5. Davis, H.E., et al., *Long COVID: major findings, mechanisms and recommendations*. Nat Rev Microbiol, 2023. **21**(3): p. 133-146.
6. Lippi, G., F. Sanchis-Gomar, and B.M. Henry, *COVID-19 and its long-term sequelae: what do we know in 2023?* Pol Arch Intern Med, 2023. **133**(4).
7. Luies, L. and I. du Preez, *The Echo of Pulmonary Tuberculosis: Mechanisms of Clinical Symptoms and Other Disease-Induced Systemic Complications*. Clin Microbiol Rev, 2020. **33**(4).
8. Loddenkemper, R., M. Lipman, and A. Zumla, *Clinical Aspects of Adult Tuberculosis*. Cold Spring Harb Perspect Med, 2015. **6**(1): p. a017848.
9. Morley, J.E., D.R. Thomas, and M.M. Wilson, *Cachexia: pathophysiology and clinical relevance*. Am J Clin Nutr, 2006. **83**(4): p. 735-43.

10. Chang, S.W., et al., *Gut hormones, appetite suppression and cachexia in patients with pulmonary TB*. PLoS One, 2013. **8**(1): p. e54564.
11. Bisht, M.K., et al., *The cause-effect relation of tuberculosis on incidence of diabetes mellitus*. Front Cell Infect Microbiol, 2023. **13**: p. 1134036.
12. Niazi, A.K. and S. Kalra, *Diabetes and tuberculosis: a review of the role of optimal glycemic control*. J Diabetes Metab Disord, 2012. **11**(1): p. 28.
13. Jensen-Cody, S.O. and M.J. Potthoff, *Hepatokines and metabolism: Deciphering communication from the liver*. Mol Metab, 2021. **44**: p. 101138.
14. Kumar, N.P., et al., *Acute Phase Proteins Are Baseline Predictors of Tuberculosis Treatment Failure*. Front Immunol, 2021. **12**: p. 731878.
15. Quinton, L.J., A.J. Walkey, and J.P. Mizgerd, *Integrative Physiology of Pneumonia*. Physiol Rev, 2018. **98**(3): p. 1417-1464.
16. Shim, D., H. Kim, and S.J. Shin, *Mycobacterium tuberculosis Infection-Driven Foamy Macrophages and Their Implications in Tuberculosis Control as Targets for Host-Directed Therapy*. Front Immunol, 2020. **11**: p. 910.
17. Park, J.H., et al., *Understanding Metabolic Regulation Between Host and Pathogens: New Opportunities for the Development of Improved Therapeutic Strategies Against Mycobacterium tuberculosis Infection*. Front Cell Infect Microbiol, 2021. **11**: p. 635335.
18. Gago, G., L. Diacovich, and H. Gramajo, *Lipid metabolism and its implication in mycobacteria-host interaction*. Curr Opin Microbiol, 2018. **41**: p. 36-42.
19. Wang, F., et al., *Organ-organ communication: The liver's perspective*. Theranostics, 2021. **11**(7): p. 3317-3330.
20. Alper, C.A., et al., *Human C'3: evidence for the liver as the primary site of synthesis*. Science, 1969. **163**(3864): p. 286-8.
21. Zhou, Z., M.J. Xu, and B. Gao, *Hepatocytes: a key cell type for innate immunity*. Cell Mol Immunol, 2016. **13**(3): p. 301-15.
22. Zhang, D., et al., *Important Hormones Regulating Lipid Metabolism*. Molecules, 2022. **27**(20).
23. Datta, D., et al., *Actionable mechanisms of drug tolerance and resistance in Mycobacterium tuberculosis*. FEBS J, 2024. **291**(20): p. 4433-4452.
24. Deb, C., et al., *A novel in vitro multiple-stress dormancy model for Mycobacterium tuberculosis generates a lipid-loaded, drug-tolerant, dormant pathogen*. PLoS One, 2009. **4**(6): p. e6077.
25. Liu, Y., et al., *Immune activation of the host cell induces drug tolerance in Mycobacterium tuberculosis both in vitro and in vivo*. J Exp Med, 2016. **213**(5): p. 809-25.
26. Samuels, A.N., et al., *Understanding the contribution of metabolism to Mycobacterium tuberculosis drug tolerance*. Front Cell Infect Microbiol, 2022. **12**: p. 958555.
27. Santucci, P., et al., *Intracellular localisation of Mycobacterium tuberculosis affects efficacy of the antibiotic pyrazinamide*. Nat Commun, 2021. **12**(1): p. 3816.

919 28. Wu, K.C. and C.J. Lin, *The regulation of drug-metabolizing enzymes and membrane*
920 *transporters by inflammation: Evidences in inflammatory diseases and age-related*
921 *disorders*. J Food Drug Anal, 2019. **27**(1): p. 48-59.
922 29. Wu, Z., et al., *Diagnosis and treatment of hepatic tuberculosis: report of five cases*
923 *and review of literature*. Int J Clin Exp Med, 2013. **6**(9): p. 845-50.
924 30. Turhan, N., et al., *Hepatic granulomas: a clinicopathologic analysis of 86 cases*.
925 Pathol Res Pract, 2011. **207**(6): p. 359-65.
926 31. Hickey, A.J., et al., *A systematic review of hepatic tuberculosis with considerations in*
927 *human immunodeficiency virus co-infection*. BMC Infect Dis, 2015. **15**: p. 209.
928 32. Celton-Morizur, S., et al., *Polyploidy and liver proliferation: central role of insulin*
929 *signaling*. Cell Cycle, 2010. **9**(3): p. 460-6.
930 33. Jain, N., et al., *Mesenchymal stem cells offer a drug-tolerant and immune-privileged*
931 *niche to Mycobacterium tuberculosis*. Nat Commun, 2020. **11**(1): p. 3062.
932 34. Lerner, T.R., et al., *Mycobacterium tuberculosis cords within lymphatic endothelial*
933 *cells to evade host immunity*. JCI Insight, 2020. **5**(10).
934 35. Kalam, H., M.F. Fontana, and D. Kumar, *Alternate splicing of transcripts shape*
935 *macrophage response to Mycobacterium tuberculosis infection*. PLoS Pathog, 2017.
936 **13**(3): p. e1006236.
937 36. Peyron, P., et al., *Foamy macrophages from tuberculous patients' granulomas*
938 *constitute a nutrient-rich reservoir for M. tuberculosis persistence*. PLoS Pathog,
939 2008. **4**(11): p. e1000204.
940 37. Beigier-Bompadre, M., et al., *Mycobacterium tuberculosis infection modulates*
941 *adipose tissue biology*. PLoS Pathog, 2017. **13**(10): p. e1006676.
942 38. Wolk, M. and M. Fedorova, *The lipid droplet lipidome*. FEBS Lett, 2024. **598**(10): p.
943 1215-1225.
944 39. Day, N.J., P. Santucci, and M.G. Gutierrez, *Host cell environments and antibiotic*
945 *efficacy in tuberculosis*. Trends Microbiol, 2024. **32**(3): p. 270-279.
946 40. Almazroo, O.A., M.K. Miah, and R. Venkataramanan, *Drug Metabolism in the Liver*.
947 Clin Liver Dis, 2017. **21**(1): p. 1-20.
948 41. Ahmed, S., et al., *Pharmacogenomics of Drug Metabolizing Enzymes and*
949 *Transporters: Relevance to Precision Medicine*. Genomics Proteomics
950 Bioinformatics, 2016. **14**(5): p. 298-313.
951 42. Fisher, C.D., et al., *Hepatic cytochrome P450 enzyme alterations in humans with*
952 *progressive stages of nonalcoholic fatty liver disease*. Drug Metab Dispos, 2009.
953 **37**(10): p. 2087-94.
954 43. Sotsuka, T., et al., *Association of isoniazid-metabolizing enzyme genotypes and*
955 *isoniazid-induced hepatotoxicity in tuberculosis patients*. In Vivo, 2011. **25**(5): p. 803-
956 12.
957 44. Cosma, C.L., D.R. Sherman, and L. Ramakrishnan, *The secret lives of the pathogenic*
958 *mycobacteria*. Annu Rev Microbiol, 2003. **57**: p. 641-76.
959 45. Bussi, C. and M.G. Gutierrez, *Mycobacterium tuberculosis infection of host cells in*
960 *space and time*. FEMS Microbiol Rev, 2019. **43**(4): p. 341-361.

46. Arnett, E., et al., *PPARgamma is critical for Mycobacterium tuberculosis induction of Mcl-1 and limitation of human macrophage apoptosis.* PLoS Pathog, 2018. **14**(6): p. e1007100.
47. Rajaram, M.V., et al., *Mycobacterium tuberculosis activates human macrophage peroxisome proliferator-activated receptor gamma linking mannose receptor recognition to regulation of immune responses.* J Immunol, 2010. **185**(2): p. 929-42.
48. Diaz, A., et al., *Studies on the contribution of PPAR Gamma to tuberculosis physiopathology.* Front Cell Infect Microbiol, 2023. **13**: p. 1067464.
49. Bechmann, L.P., et al., *The interaction of hepatic lipid and glucose metabolism in liver diseases.* J Hepatol, 2012. **56**(4): p. 952-64.
50. Lovewell, R.R., C.M. Sassetti, and B.C. VanderVen, *Chewing the fat: lipid metabolism and homeostasis during M. tuberculosis infection.* Curr Opin Microbiol, 2016. **29**: p. 30-6.
51. Lu, J.F., et al., *GDF15 is a major determinant of ketogenic diet-induced weight loss.* Cell Metab, 2024. **36**(2): p. 454-456.
52. Rey-Bedon, C., et al., *CYP450 drug inducibility in NAFLD via an in vitro hepatic model: Understanding drug-drug interactions in the fatty liver.* Biomed Pharmacother, 2022. **146**: p. 112377.
53. Dookie, N., et al., *Evolution of drug resistance in Mycobacterium tuberculosis: a review on the molecular determinants of resistance and implications for personalized care.* J Antimicrob Chemother, 2018. **73**(5): p. 1138-1151.
54. Shiloh, M.U., *Mechanisms of mycobacterial transmission: how does Mycobacterium tuberculosis enter and escape from the human host.* Future Microbiol, 2016. **11**(12): p. 1503-1506.
55. Coleman, M., et al., *Mycobacterium tuberculosis Transmission in High-Incidence Settings-New Paradigms and Insights.* Pathogens, 2022. **11**(11).
56. Wei, X., et al., *The clinical features and prognostic factors of miliary tuberculosis in a high tuberculosis burden area.* Ann Med, 2024. **56**(1): p. 2356647.
57. McMullan, G.S. and J.H. Lewis, *Tuberculosis of the Liver, Biliary Tract, and Pancreas.* Microbiol Spectr, 2017. **5**(1).
58. Seiler, P., et al., *Limited mycobacterial infection of the liver as a consequence of its microanatomical structure causing restriction of mycobacterial growth to professional phagocytes.* Infect Immun, 2001. **69**(12): p. 7922-6.
59. Hess, S., et al., *In vivo partial reprogramming by bacteria promotes adult liver organ growth without fibrosis and tumorigenesis.* Cell Rep Med, 2022. **3**(11): p. 100820.
60. Barreto, E.A., et al., *COVID-19-related hyperglycemia is associated with infection of hepatocytes and stimulation of gluconeogenesis.* Proc Natl Acad Sci U S A, 2023. **120**(21): p. e2217119120.
61. Mercado-Gomez, M., et al., *The spike of SARS-CoV-2 promotes metabolic rewiring in hepatocytes.* Commun Biol, 2022. **5**(1): p. 827.
62. Hazlehurst, J.M., et al., *Non-alcoholic fatty liver disease and diabetes.* Metabolism, 2016. **65**(8): p. 1096-108.
63. Dharmalingam, M. and P.G. Yamasandhi, *Nonalcoholic Fatty Liver Disease and Type 2 Diabetes Mellitus.* Indian J Endocrinol Metab, 2018. **22**(3): p. 421-428.

1005 64. Toda, G., et al., *Preparation and culture of bone marrow-derived macrophages from*
1006 *mice for functional analysis*. STAR Protoc, 2021. **2**(1): p. 100246.
1007 65. Bligh, E.G. and W.J. Dyer, *A rapid method of total lipid extraction and purification*. Can
1008 J Biochem Physiol, 1959. **37**(8): p. 911-7.

1009

1010 **Main Figure legends:**

1011 **Figure 1: Presence of Mtb in human miliary tuberculosis patients:**

1012 **(A)** Hematoxylin and eosin (H and E) staining of the human autopsied liver tissue sections
1013 showing the presence of granuloma-like structure in the Mtb infected liver. **(B)** Acid-fast
1014 staining shows the presence of Mtb in the liver section of miliary TB patients. (arrows
1015 point to the presence of Mtb in the enlarged image) **(C-D)** Auramine O-Rhodamine B (A-
1016 O) staining and fluorescence in-situ hybridization (FISH) with Mtb specific 16s rRNA
1017 primer further confirms the presence of Mtb in human liver tissue sections. **(E).** Dual
1018 staining of β-actin (green) and Ag85B (red) using respective antibodies shows the
1019 presence of Mtb in hepatocytes of human biopsied liver sections. **(F).** Dual staining of β-
1020 actin (green) and Ag85B (red) using respective antibodies shows no distinct signal of
1021 Ag85B in the uninfected liver biopsied sample (control).

1022

1023 **Figure 2: Involvement of the liver and hepatocytes in a mouse aerosol model of Mtb**
1024 **infection.**

1025 **(A).** Schematic denoting the flow of experimental set up of studying the liver at tissue level
1026 and cellular level (generated by Biorender.com). **(B)** C57BL/6 mice were infected with 200
1027 CFU of H37Rv through the aerosol route and the bacterial burden of the lung and liver
1028 was enumerated at different time points post-infection in lung and spleen **(C).** Alexa Fluor
1029 488 Phalloidin and DAPI staining of uninfected and infected lungs at 8 weeks post-
1030 infection. Images were taken in 40 X magnification as mentioned (scale bar is 20 μm).
1031 **(D).** Immunofluorescence staining of Alexa Fluor 488 Phalloidin, DAPI, and Ag85B in the
1032 infected mice liver at 8 weeks post-infection shows the presence of Ag85B signals within
1033 hepatocytes (magnified image) (scale bar is 20 μm). **(E).** Isolated primary hepatocytes
1034 stained with phalloidin green and DAPI show the typical polygonal shape with binucleated

1035 morphology. **(F).** Anti-asialoglycoprotein receptor (ASGR1) antibody staining specifically
1036 stains primary hepatocytes isolated from infected mice as validated by the contour plot in
1037 flow cytometry. **(G).** Antiasialoglycoprotein receptor (ASGR1) antibody staining
1038 specifically stains primary hepatocytes isolated from mice as visualized through confocal
1039 microscopy. **(H).** Primary hepatocytes were isolated from the infected mice, lysed and
1040 CFU enumeration was done at the mentioned time points. **(I).** Ag85B staining of cultured
1041 primary hepatocytes, isolated from mice at 8 weeks post Mtb infection. (scale bar is 20
1042 µm). **(J).** Dual immunostaining of Ag85B (red) and albumin (green) shows distinct signals
1043 of Mtb within the isolated hepatocytes from infected mice at 8 weeks post-infection. (n)=
1044 6-7 mice in each group.

1045

1046 **Figure 3: Mtb uses hepatocytes as a replicative niche:**

1047 **(A and B).** Representative microscopic images showing the infection of primary
1048 hepatocytes (PHCs), AML-12, HepG2, and Huh-7 with labelled Mtb-H37Rv strains and
1049 subsequent quantification of percentage infectivity in the respective cell types. RAW
1050 264.7, THP-1 and murine BMDMs were used as macrophage controls. The scale bar in
1051 all images is 10 µm except in HepG2, which is 5 µm **(C).** CFU enumeration of Mtb-H37Rv
1052 in different hepatic cell lines. **(D and E).** Representative confocal microscopy images of
1053 Mtb-GFP-H37Rv infected PHCs at the respective time points post-infection and bar blot
1054 depicting mean fluorescent intensity (MFI) / cell at the respective time points. **(F and G).**
1055 Representative confocal microscopy images of MtbH37Rv-GFP infected HepG2 at the
1056 respective time points post-infection and bar blot depicting MFI/cell at the respective time
1057 points, n= 4 independent experiments, with each dot representing 5 fields of 30-60 cells.
1058 Scale bar 10 µm. (**H).** Fold change of growth rate of Mtb within HepG2, PHCs, RAW
1059 264.7, THP-1 and BMDMs at the mentioned time points post-infection.

1060

1061

1062

1063 **Figure 4: RNA sequence analysis of infected and sorted hepatocytes at 0 hours and**
1064 **48 hours post-infection:**

1065 **(A).** Experimental setup for infection of HepG2 with Mb-H37Rv-mCherry at 10 MOI with
1066 histogram of mCherry signals at 0- and 48-hours post-infection (Schematic depicting
1067 experimental set up generated with Biorender.com) **(B).** Principal component analysis
1068 (PCA) plot illustrating the HepG2 transcriptome, identified through global transcriptomic
1069 analysis of 0 hours uninfected and infected and 48 hours uninfected and infected. **(C).**
1070 GO pathway enrichment analysis was done for DEGs with adjusted p-value < 0.05 at 0-
1071 and 48-hours post-infection. The bubble plot depicts the enrichment of pathways on the
1072 mentioned time points post-infection, where the coordinate on the x-axis represents the
1073 gene ratio, the bubble size represents the gene count and colour represents the p-value.
1074 **(D and E).** Volcano plot depicting the fold change of different genes in 0 hours and 48
1075 hours post-infection, the red dots represent the significantly upregulated and
1076 downregulated genes.

1077

1078 **Figure 5: Increased fatty acid biogenesis drives Mtb growth in hepatocytes:**

1079 **(A)**. Increased number of LDs/cells in HepG2 and PHCs post-Mtb infection as compared
1080 to the uninfected cells **(B).** Quantification of the number of lipid droplets in the infected
1081 HepG2 and PHCs with their uninfected control, 50-70 cells were analyzed from 3
1082 independent experiments. **(C).** Increase in the BODIPY intensity at different days post-
1083 infection in infected hepatocytes **(D)**. A high degree of colocalization of Mtb-*H37Rv*-GFP
1084 (green) with lipid droplets (red) within PHCs **(E)** Mass spectrometric quantification of the
1085 different species of DAGs, TAGs, and cholesterol esters in the Mtb infected
1086 hepatocytes. **(F)**. Confocal images showing puncta of fluorescently labelled fatty acid in
1087 Mtb derived from metabolically labelled (with BODIPY 558/568 C_{12}) HepG2. Relative CFU
1088 of Mtb under the administration of different inhibitors of the lipid metabolic pathway in **(G)**.
1089 PHCs **(H)**. HepG2 and **(I)**. THP-1. Representative data from 3 independent experiments.
1090 Data were analyzed using the two-tailed unpaired Student's t-test in B and one-way
1091 ANOVA in C, F, G, and H.*p < 0.05, **p < 0.005, ***p < 0.0005, ****p < 0.0001. ns=non-
1092 significant.

1093 **Figure 6: PPARγ driven lipid biogenesis drives Mtb growth in hepatocytes:**

1094 **(A)** Heat map showing the fold change of the genes involved in the lipid biosynthesis and
1095 LD biogenesis in liver across weeks 2, 4 and 8, post infection. **(B)** Kinetic increase in the
1096 gene expression of *Pparγ* transcript levels across different weeks post
1097 infection **(C)** Immunoblot showing increased PPARγ in PHCs (MOI: 10) at 5-, 24- and 48-
1098 hours post-infection. **(D)** Bar plot showing the increased band intensity of PPARγ in the
1099 infected PHCs at the mentioned time points. **(E)** Representative confocal microscopy
1100 images showing HepG2 infected with Mtb-mCherry-*H37Rv* and treated with GW9662 and
1101 rosiglitazone **(F)** MFI/cell of in Mtb-mCherry-*H37Rv* DMSO treated, GW9662 and
1102 rosiglitazone treated HepG2 cells. **(G)** Representative confocal images of uninfected,
1103 infected, GW9662 and rosiglitazone treated infected HepG2 showing changes in the
1104 number of LDs. **(H)** Plot depicting the quantification of LDs/cell in the mentioned
1105 conditions. Representative data from n=4 biological replicates. Data were analysed by
1106 using the two tailed unpaired Student's t test in D and by one way ANOVA in B, F and H.
1107 *$p < 0.05$, **$p < 0.005$, ***$p < 0.0005$, ****$p < 0.0001$, ns=non-significant

1108

1109 **Figure 7: Hepatocytes provide a drug-tolerant niche to Mtb:**

1110 **(A).** Experimental scheme of deducting the percentage drug tolerance in hepatocytes
1111 (generated with Biorender.com) **(B).** Percentage tolerance of Mtb-H37Rv against
1112 Rifampicin within RAW 264.7, PHCs and HepG2 at different time points post-
1113 infection. **(C).** Percentage tolerance of Mtb-H37Rv against Isoniazid within RAW 264.7,
1114 PHCs, and HepG2 at different time points post-infection. Representative data from 3
1115 independent experiments. **(D).** Percentage tolerance of Mtb-*H37Rv* against rifampicin
1116 within BMDMs, PHCs, and HepG2 as measured microscopically (**E).** Percentage
1117 tolerance of Mtb-H37Rv against isoniazid within BMDMs, PHCs, and HepG2 measured
1118 microscopically. Representative data from 3 independent experiments. Each dot
1119 represents a single field having more than 4 infected cells. 20 such fields were
1120 analyzed **(F)**. Transcript levels of the various DMEs involved in Rifampicin and Isoniazid
1121 metabolism in mice liver, 8 weeks post-infection (n=4 mice), the fold change has been
1122 calculated by considering the expression in the uninfected mice to be 1. Data were

1123 analyzed by using 2-way ANOVA in (B) and (C), one-way ANOVA in (D) and (E) and the
1124 two-tailed unpaired Student's t-test in (F) and Representative data from n=4 biological
1125 replicates *p < 0.05, **p < 0.005, ***p < 0.0005, ****p < 0. 0001.ns=non-significant.

1126

1127

1128

1129

1130

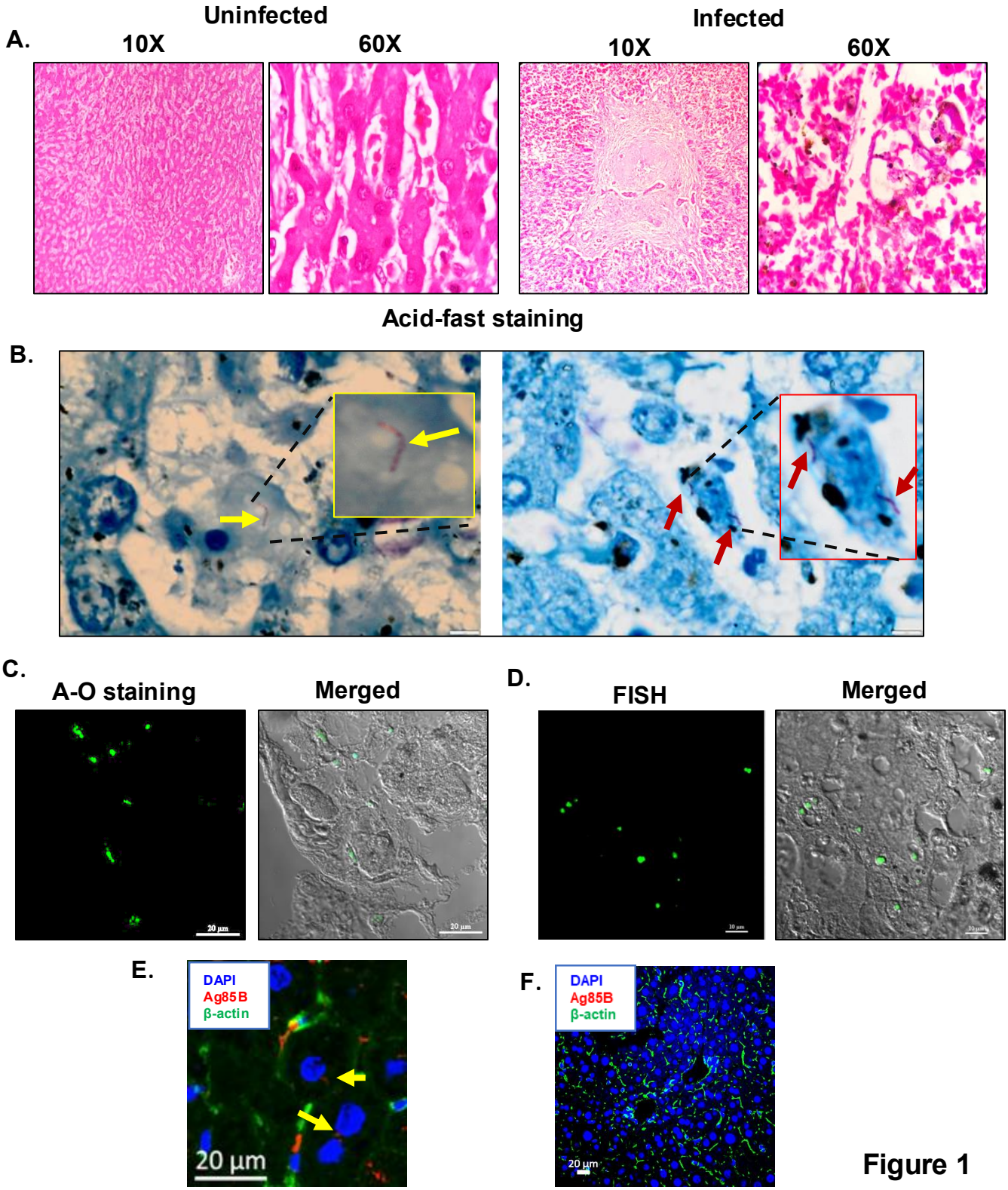
A.
Uninfected
10X
60X
Infected
10X
60X
Acid-fast staining
B.
C.
A-O staining
Merged
D.
FISH
Merged
E.
DAPI
Ag85B
β-actin
20 µm
F.
DAPI
Ag85B
β-actin
20 µm

Figure 1

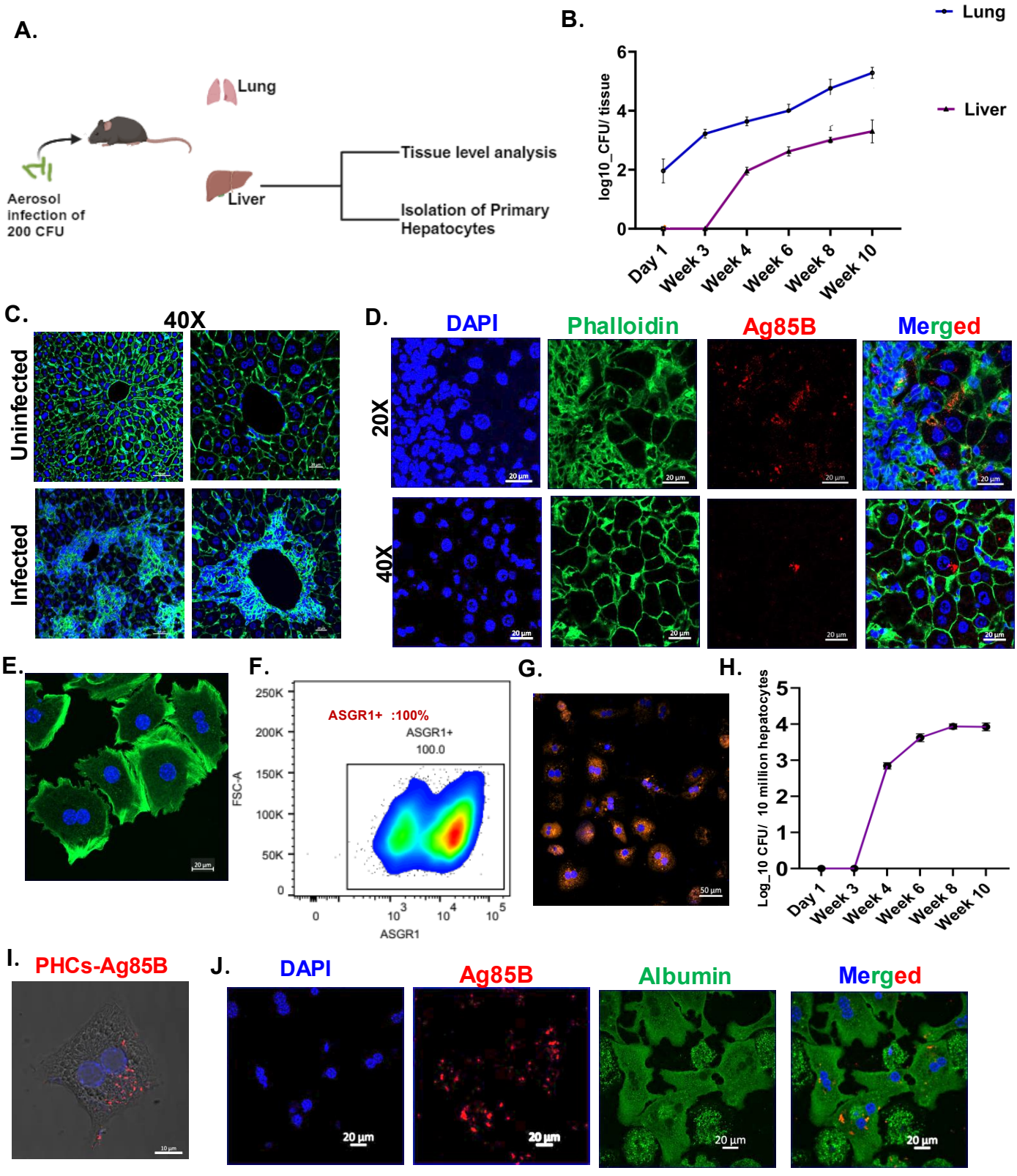
A.
Lung
Liver
Aerosol infection of 200 CFU
Tissue level analysis
Isolation of Primary Hepatocytes
B.
Lung
Liver
log10_CFU/ tissue
Day 1
Week 3
Week 4
Week 6
Week 8
Week 10
C.
40X
Uninfected
Infected
D.
DAPI
Phalloidin
Ag85B
Merged
20X
40X
E.
F.
ASGR1+ :100%
ASGR1+
100.0
FSC-A
ASGR1
G.
H.
Log_10 CFU/ 10 million hepatocytes
I.
PHCs-Ag85B
J.
DAPI
Ag85B
Albumin
Merged
20 µm

Figure 2

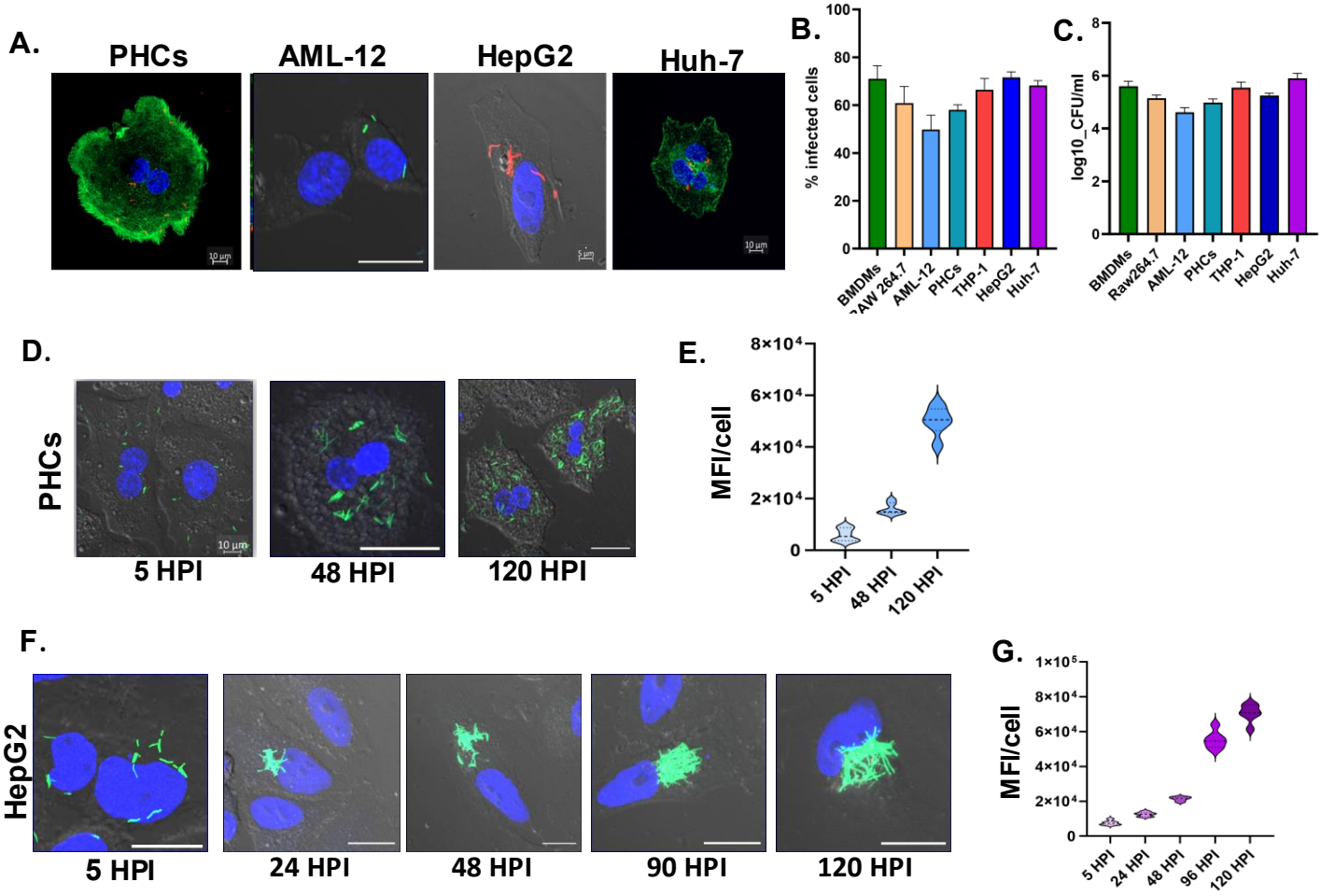
A.
PHCs
AML-12
HepG2
Huh-7
B.
% infected cells
BMDMs
RAW 264.7
AML-12
PHCs
THP-1
HepG2
Huh-7
C.
log10_CFU/ml
BMDMs
Raw264.7
AML-12
PHCs
THP-1
HepG2
Huh-7
D.
PHCs
5 HPI
48 HPI
120 HPI
E.
MFI/cell
5 HPI
48 HPI
120 HPI
F.
HepG2
5 HPI
24 HPI
48 HPI
90 HPI
120 HPI
G.
MFI/cell
5 HPI
24 HPI
48 HPI
96 HPI
120 HPI

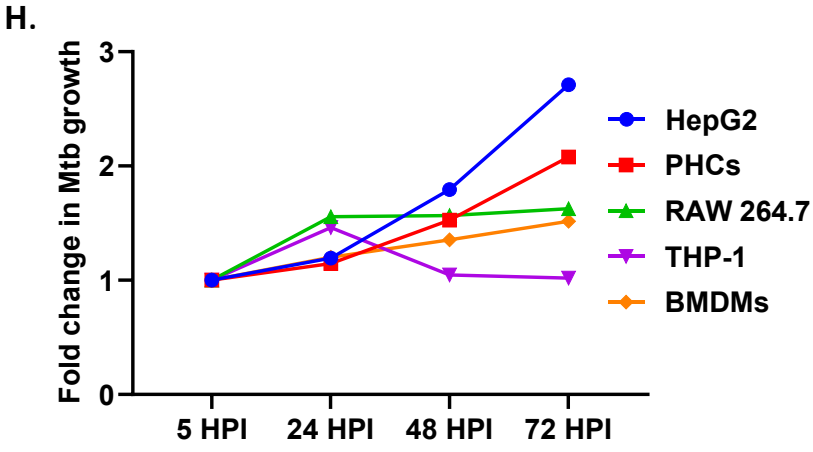
H.
Fold change in Mtb growth
5 HPI
24 HPI
48 HPI
72 HPI
HepG2
PHCs
RAW 264.7
THP-1
BMDMs

Figure 3

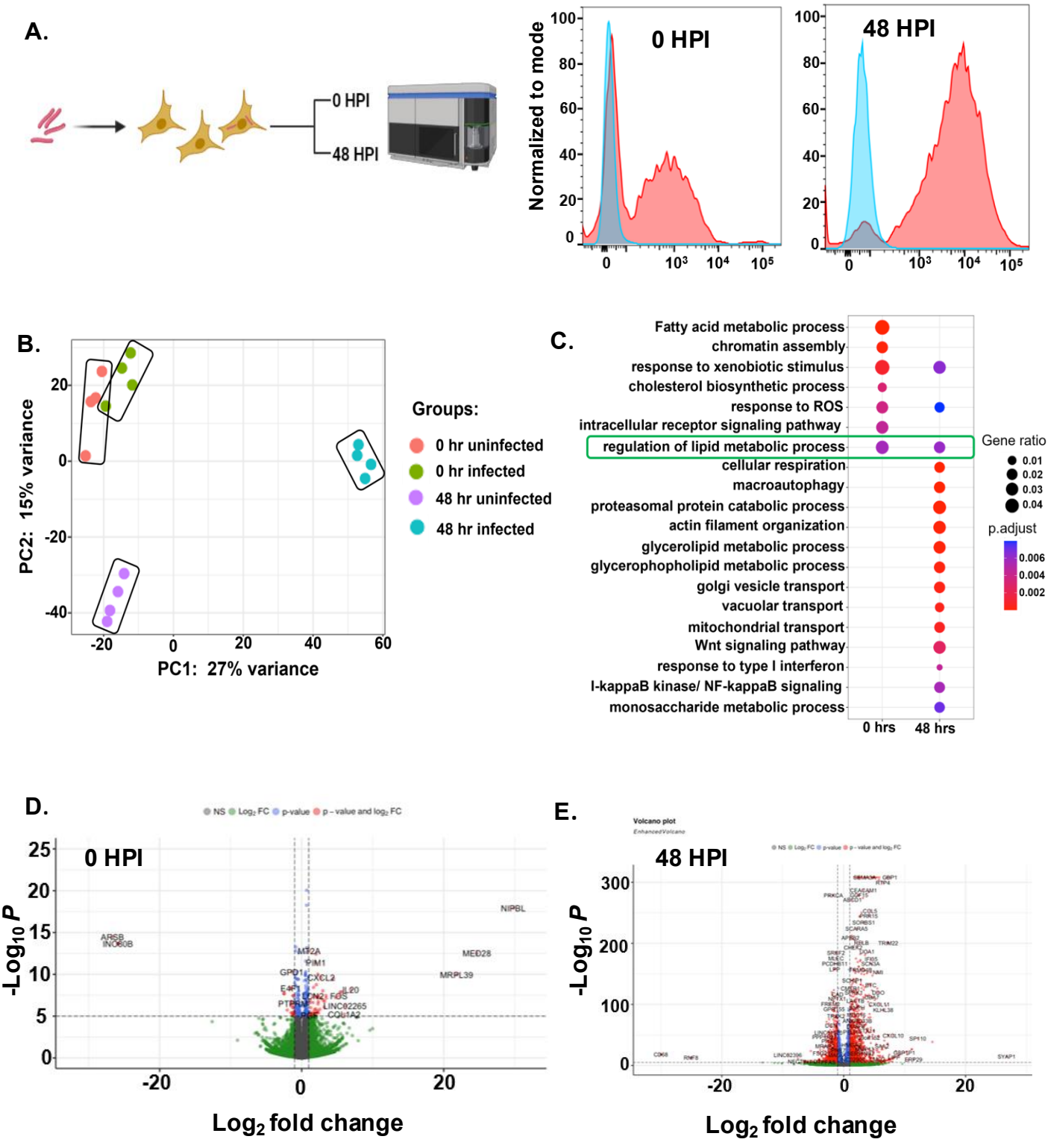
A.
0 HPI
48 HPI
Normalized to mode
0 HPI
48 HPI
B.
PC2: 15% variance
PC1: 27% variance
Groups:
0 hr uninfected
0 hr infected
48 hr uninfected
48 hr infected
C.
Fatty acid metabolic process
chromatin assembly
response to xenobiotic stimulus
cholesterol biosynthetic process
response to ROS
intracellular receptor signaling pathway
regulation of lipid metabolic process
cellular respiration
macroautophagy
proteasomal protein catabolic process
actin filament organization
glycerolipid metabolic process
glycerophopholipid metabolic process
golgi vesicle transport
vacuolar transport
mitochondrial transport
Wnt signaling pathway
response to type I interferon
I-kappaB kinase/ NF-kappaB signaling
monosaccharide metabolic process
0 hrs
48 hrs
Gene ratio
p.adjust
D.
0 HPI
-Log10 P
Log2 fold change
E.
48 HPI
-Log10 P
Log2 fold change

Figure 4

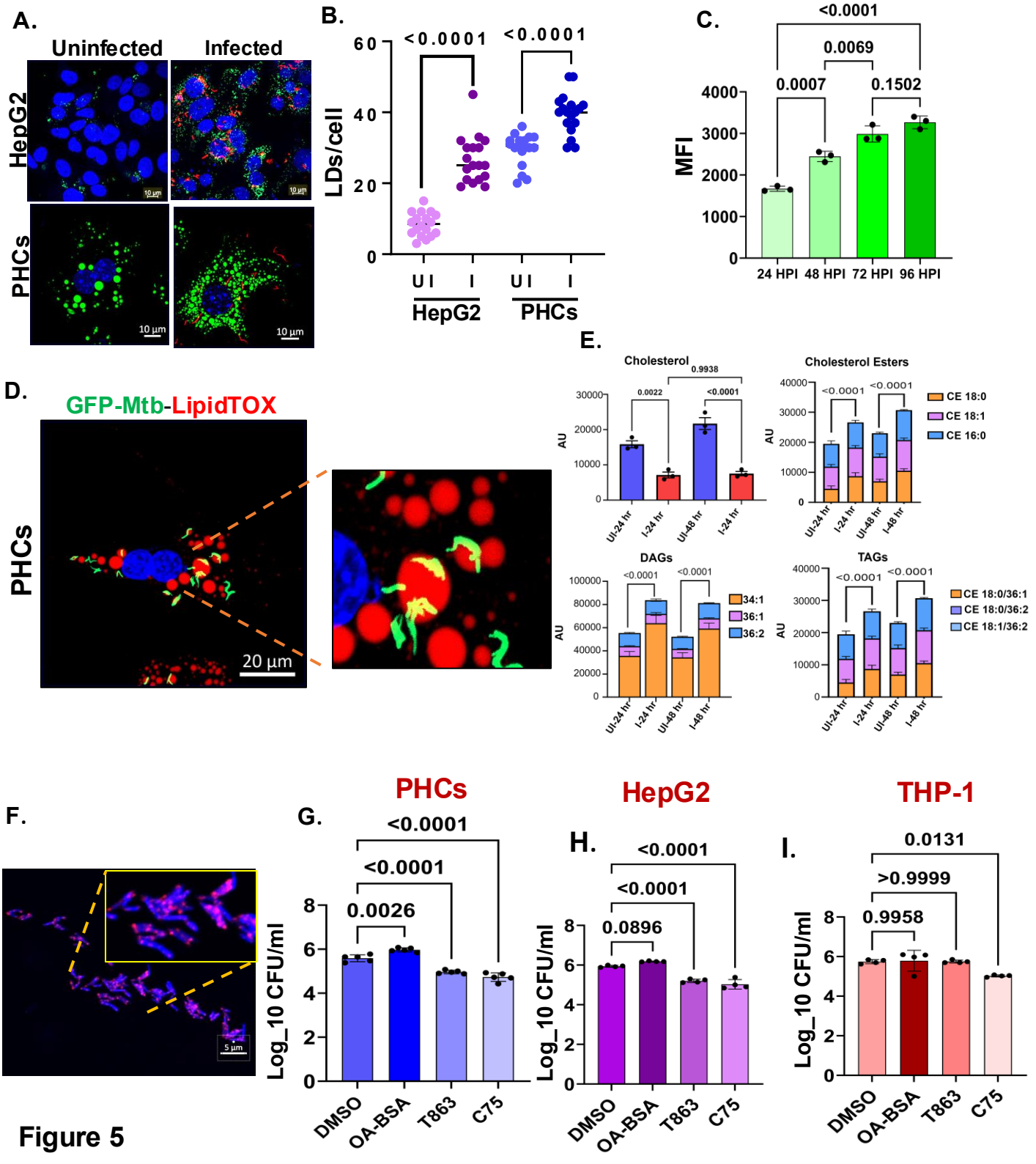
A.
Uninfected
Infected
HepG2
PHCs
10 µm
B.
LDs/cell
<0.0001
<0.0001
U I
I
HepG2
PHCs
C.
MFI
<0.0001
0.0069
0.0007
0.1502
24 HPI
48 HPI
72 HPI
96 HPI
D.
GFP-Mtb-LipidTOX
PHCs
20 µm
E.
Cholesterol
Cholesterol Esters
DAGs
TAGs
AU
0.0022
0.9938
<0.0001
CE 18:0
CE 18:1
CE 16:0
34:1
36:1
36:2
CE 18:0/36:1
CE 18:0/36:2
CE 18:1/36:2
UI-24 hr
I-24 hr
UI-48 hr
I-48 hr
F.
5 µm
PHCs
HepG2
THP-1
G.
H.
I.
Log_10 CFU/ml
<0.0001
<0.0001
0.0026
0.0896
0.0131
>0.9999
0.9958
DMSO
OA-BSA
T863
C75

Figure 5

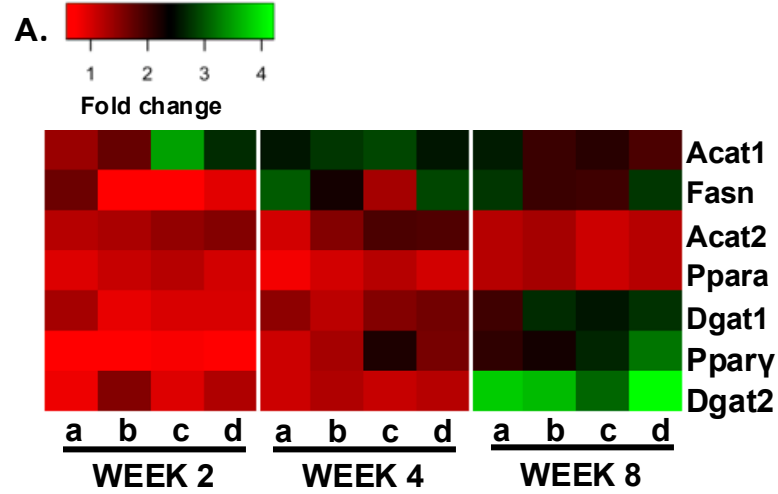
A.
1
2
3
4
Fold change
Acat1
Fasn
Acat2
Ppara
Dgat1
Pparγ
Dgat2
a b c d
a b c d
a b c d
WEEK 2
WEEK 4
WEEK 8

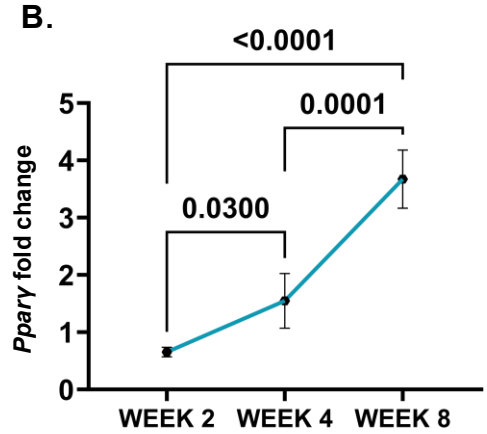
B.
<0.0001
0.0001
0.0300
Ppary fold change
0
1
2
3
4
5
WEEK 2
WEEK 4
WEEK 8

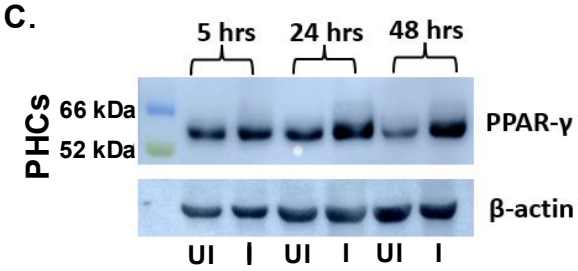
C.
5 hrs
24 hrs
48 hrs
PHCs
66 kDa
52 kDa
PPAR-γ
β-actin
UI I UI I UI I

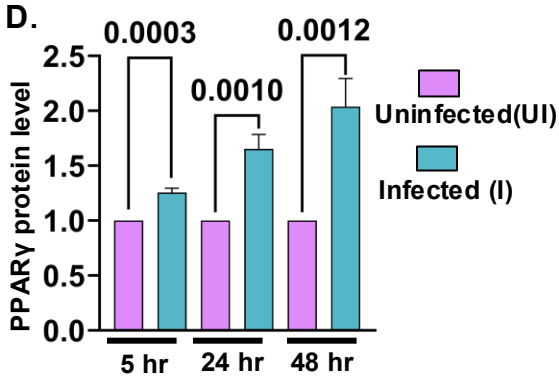
D.
0.0003
0.0012
0.0010
PPARγ protein level
0.0
0.5
1.0
1.5
2.0
2.5
Uninfected(UI)
Infected (I)
5 hr
24 hr
48 hr

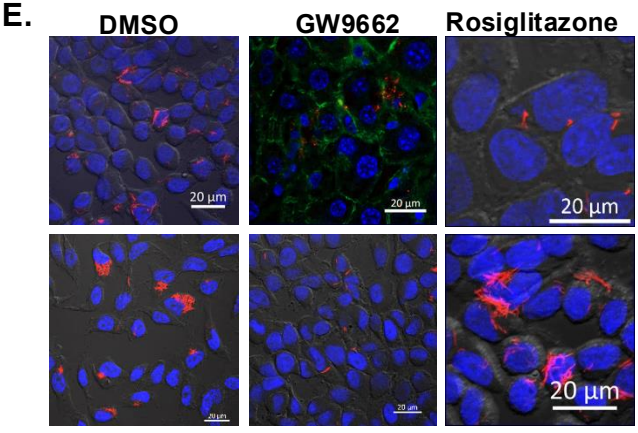
E.
DMSO
GW9662
Rosiglitazone
20 µm
20 µm
20 µm
20 µm
20 µm
20 µm

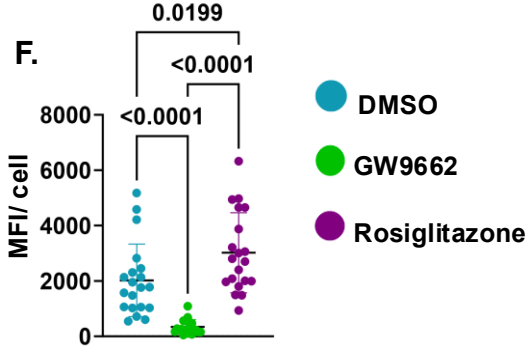
F.
0.0199
<0.0001
<0.0001
MFI/ cell
0
2000
4000
6000
8000
DMSO
GW9662
Rosiglitazone

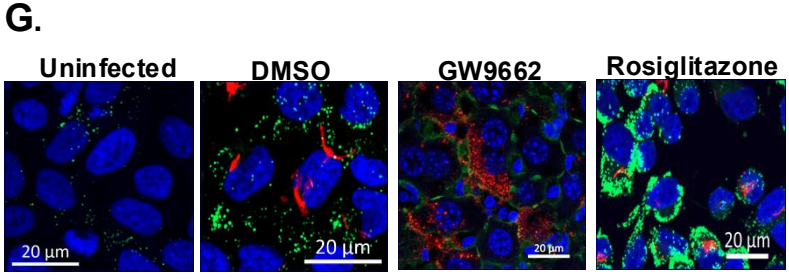
G.
Uninfected
DMSO
GW9662
Rosiglitazone
20 µm
20 µm
20 µm
20 µm

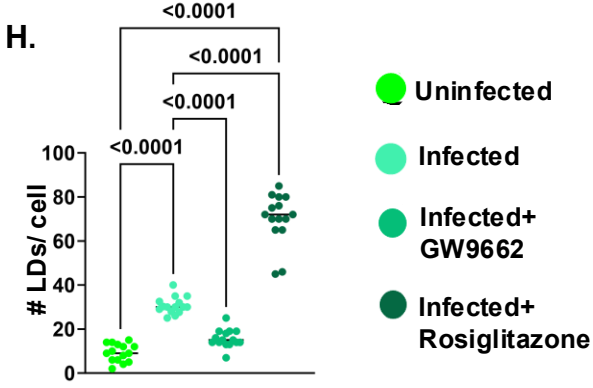
H.
<0.0001
<0.0001
<0.0001
<0.0001
LDs/ cell
0
20
40
60
80
100
Uninfected
Infected
Infected+ GW9662
Infected+ Rosiglitazone

Figure 6

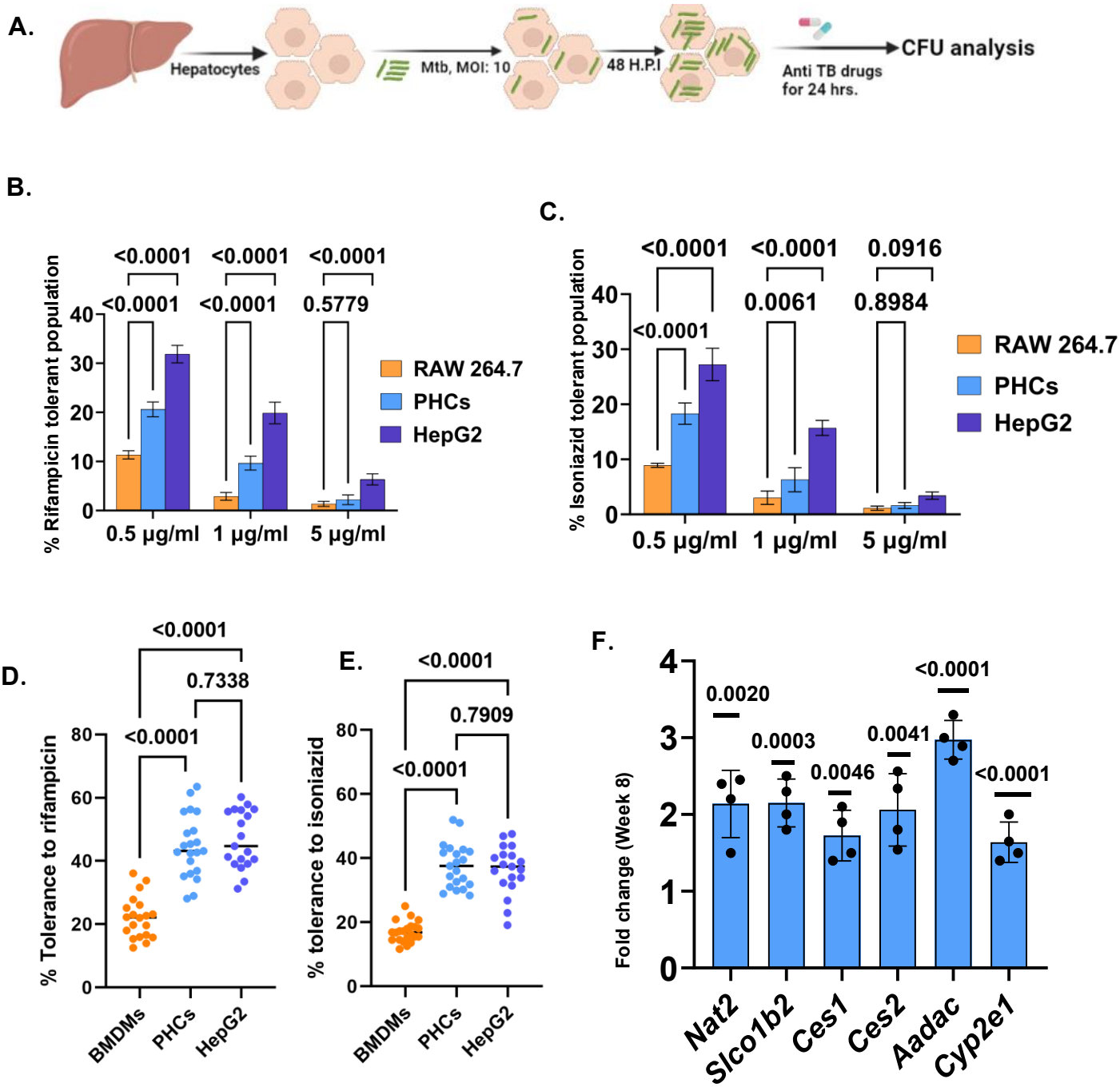
A.
Hepatocytes
Mtb, MOI: 10
48 H.P.I
Anti TB drugs
for 24 hrs.
CFU analysis
B.
% Rifampicin tolerant population
<0.0001
<0.0001
<0.0001
<0.0001
<0.0001
0.5779
RAW 264.7
PHCs
HepG2
0.5 µg/ml
1 µg/ml
5 µg/ml
C.
% Isoniazid tolerant population
<0.0001
<0.0001
0.0916
<0.0001
0.0061
0.8984
RAW 264.7
PHCs
HepG2
0.5 µg/ml
1 µg/ml
5 µg/ml
D.
% Tolerance to rifampicin
<0.0001
0.7338
<0.0001
BMDMs
PHCs
HepG2
E.
% tolerance to isoniazid
<0.0001
0.7909
<0.0001
BMDMs
PHCs
HepG2
F.
Fold change (Week 8)
0.0020
0.0003
0.0046
0.0041
<0.0001
<0.0001
Nat2
Slco1b2
Ces1
Ces2
Aadac
Cyp2e1

Figure 7

Supplementary data for the manuscript **‘’PPARγ mediated lipid biogenesis fuels *Mycobacterium tuberculosis* growth in a drug-tolerant hepatocyte environment” (REVISED)**

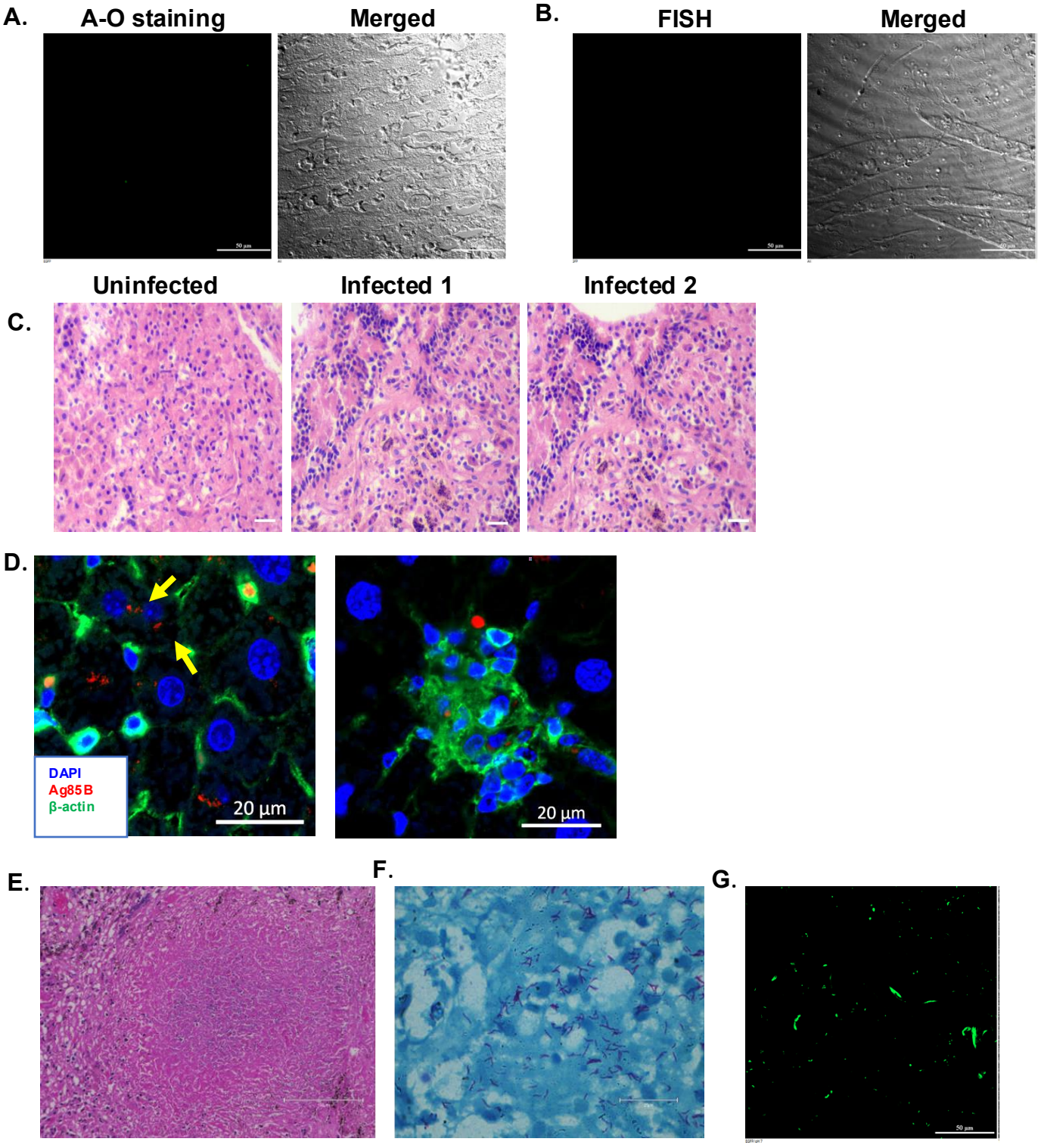

Figure 1, Supplementary

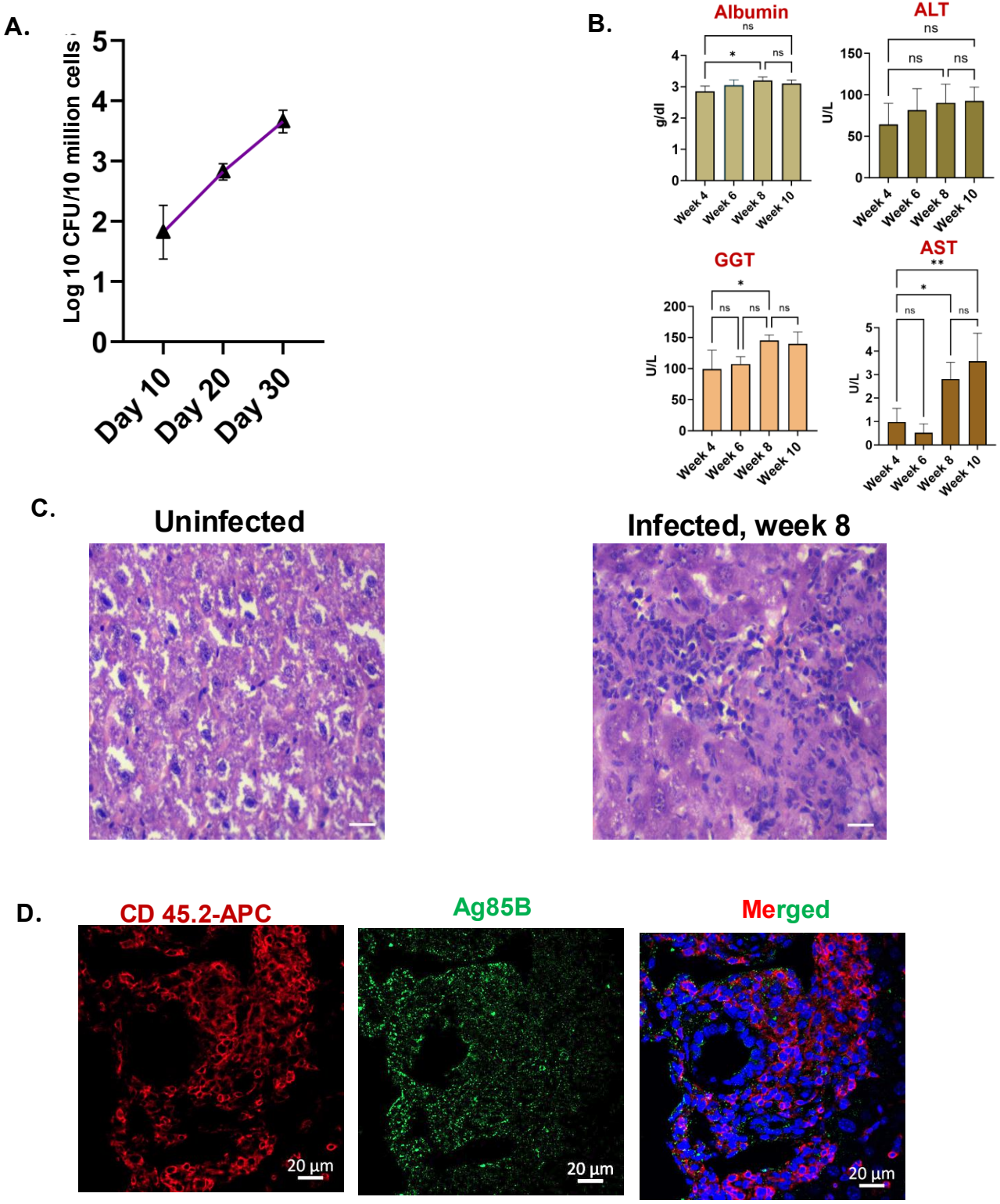

Figure 2, Supplementary

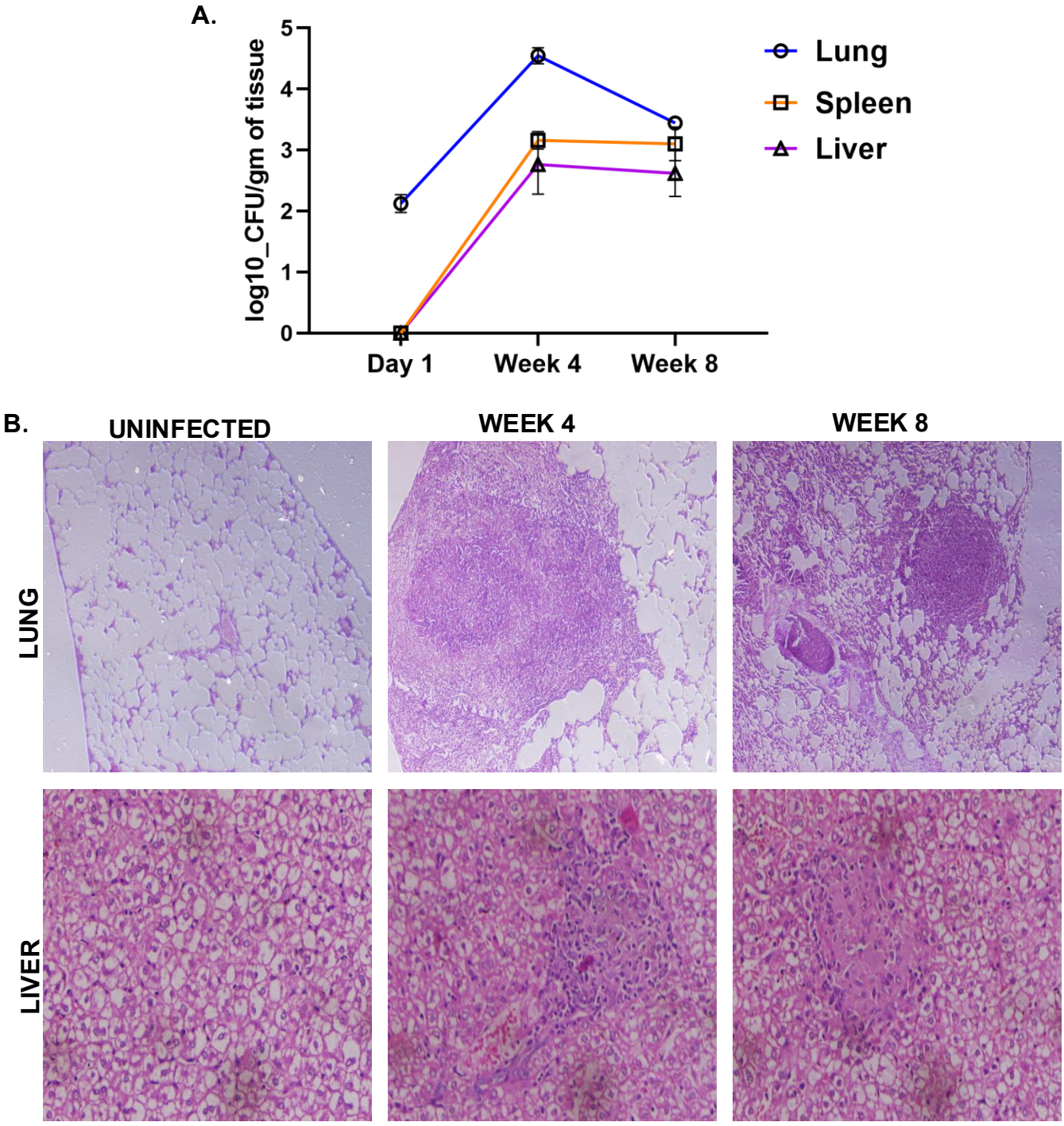

Figure 3, Supplementary

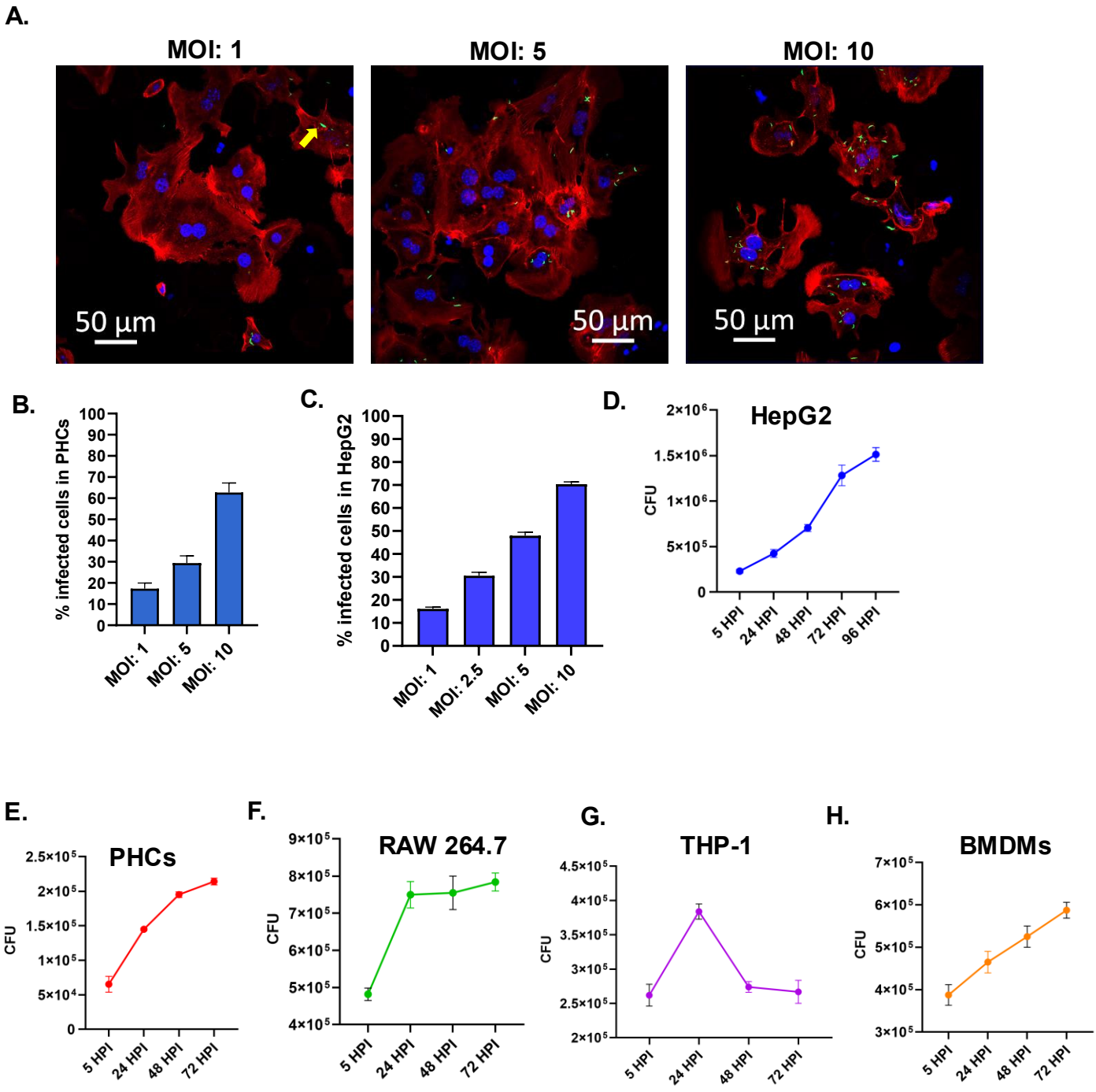

Figure 4, Supplementary

A. Dot Plot of GO Term Enrichment for THP-1, infected with Mtb 48 HPI

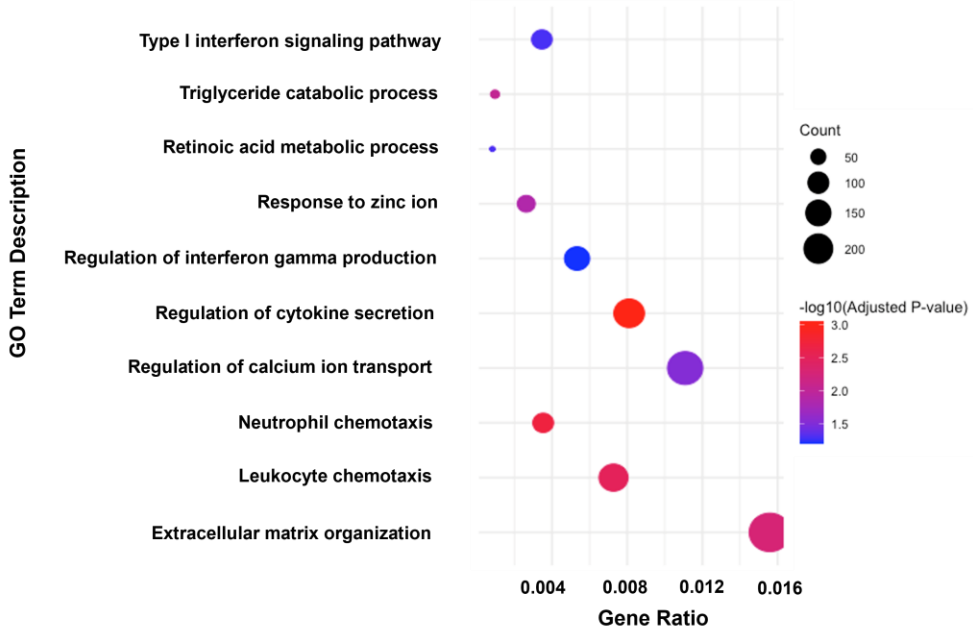

B. Dot Plot of GO Term Enrichment for HepG2, infected with Mtb 48 HPI

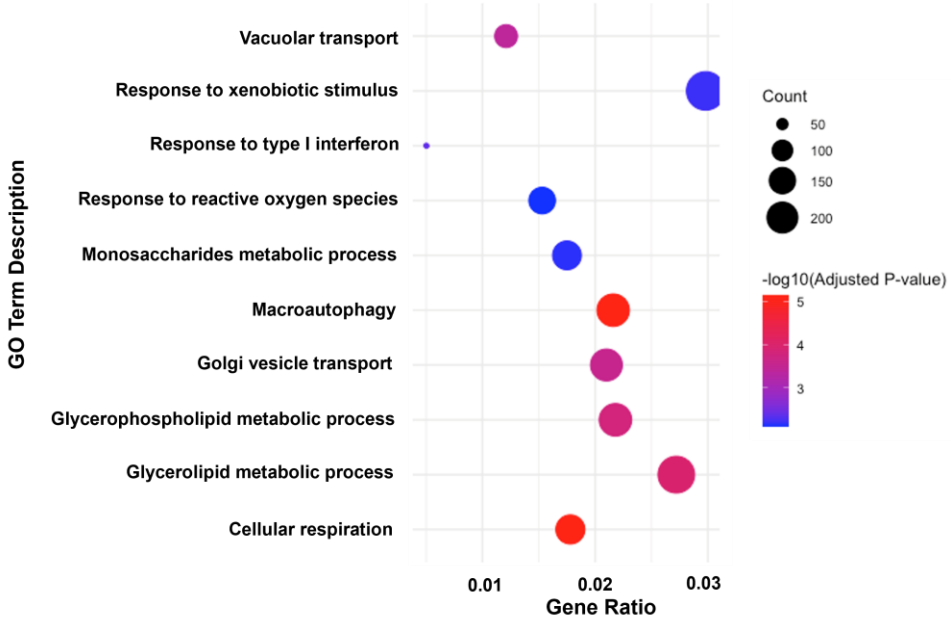

Figure 5, Supplementary

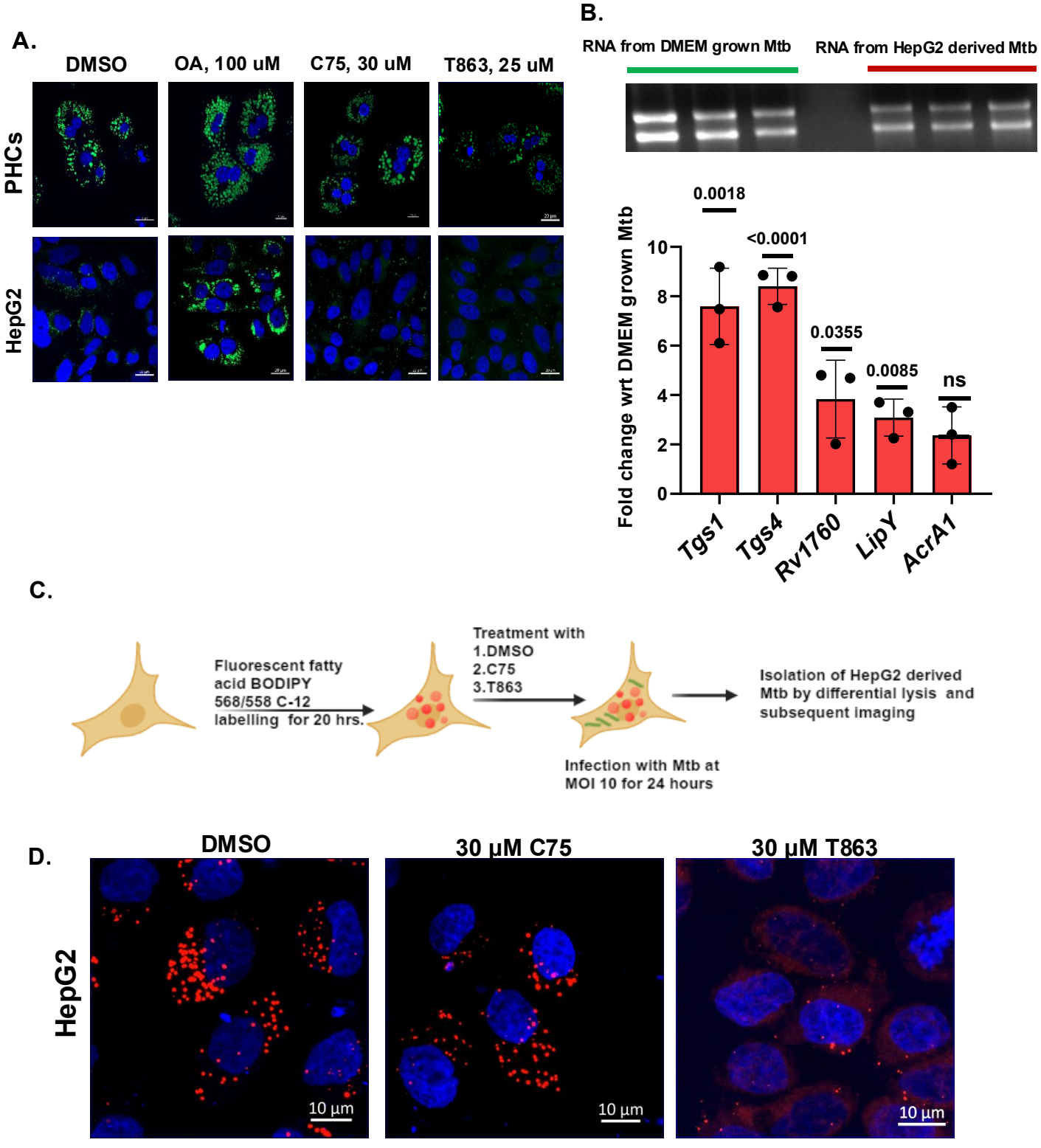

Figure 6, Supplementary

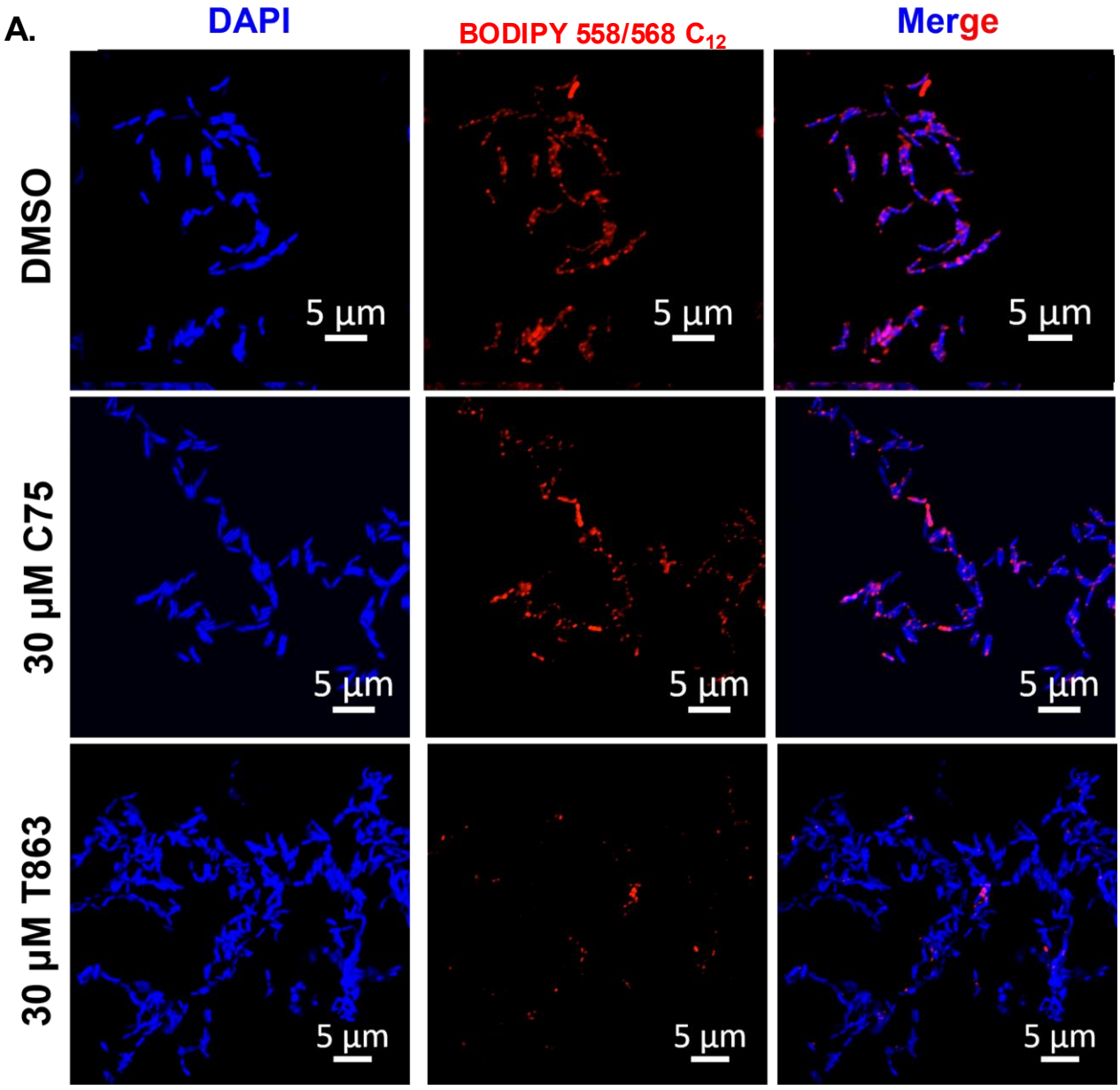

Figure 7, Supplementary

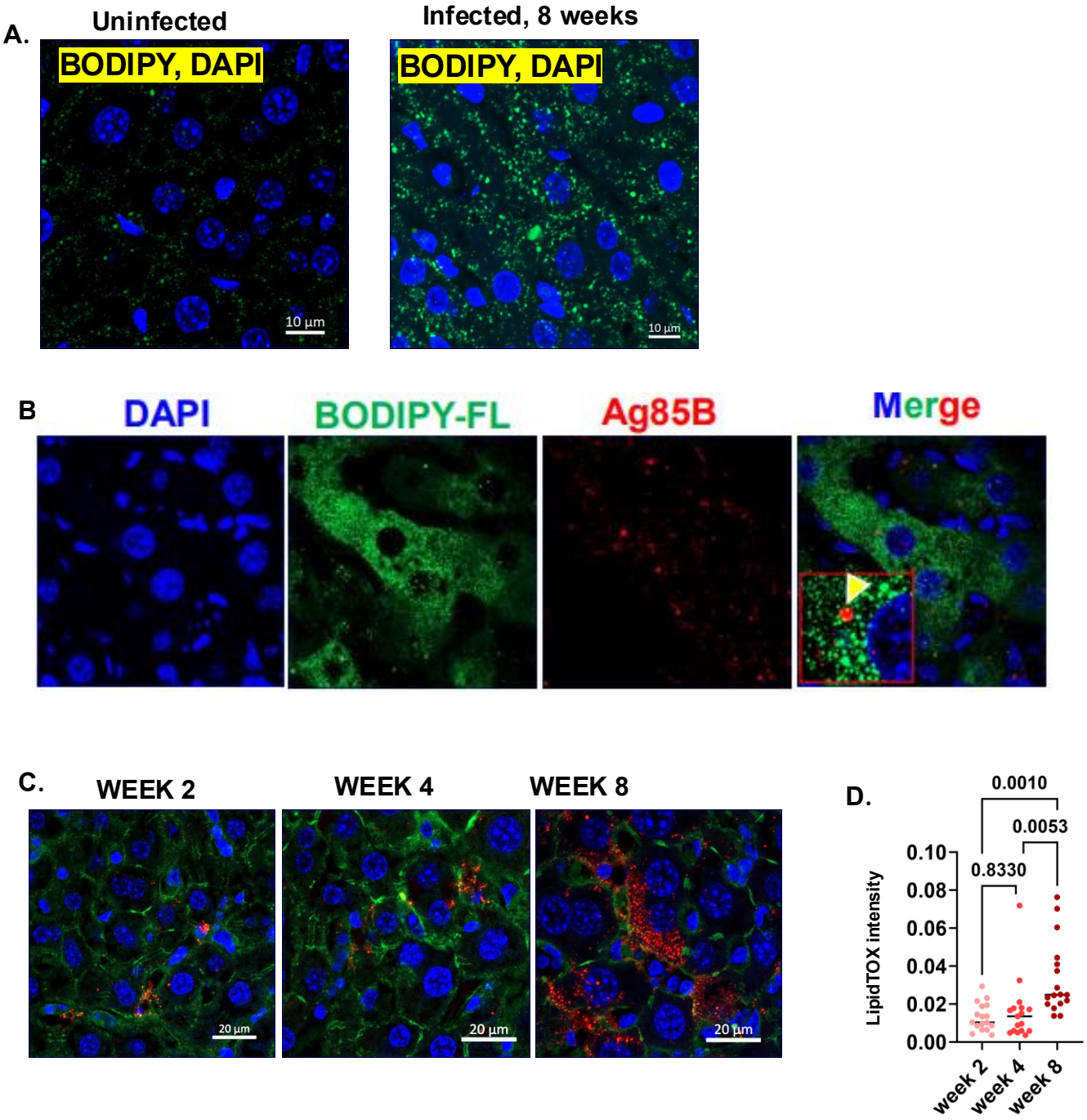

Figure 8, Supplementary

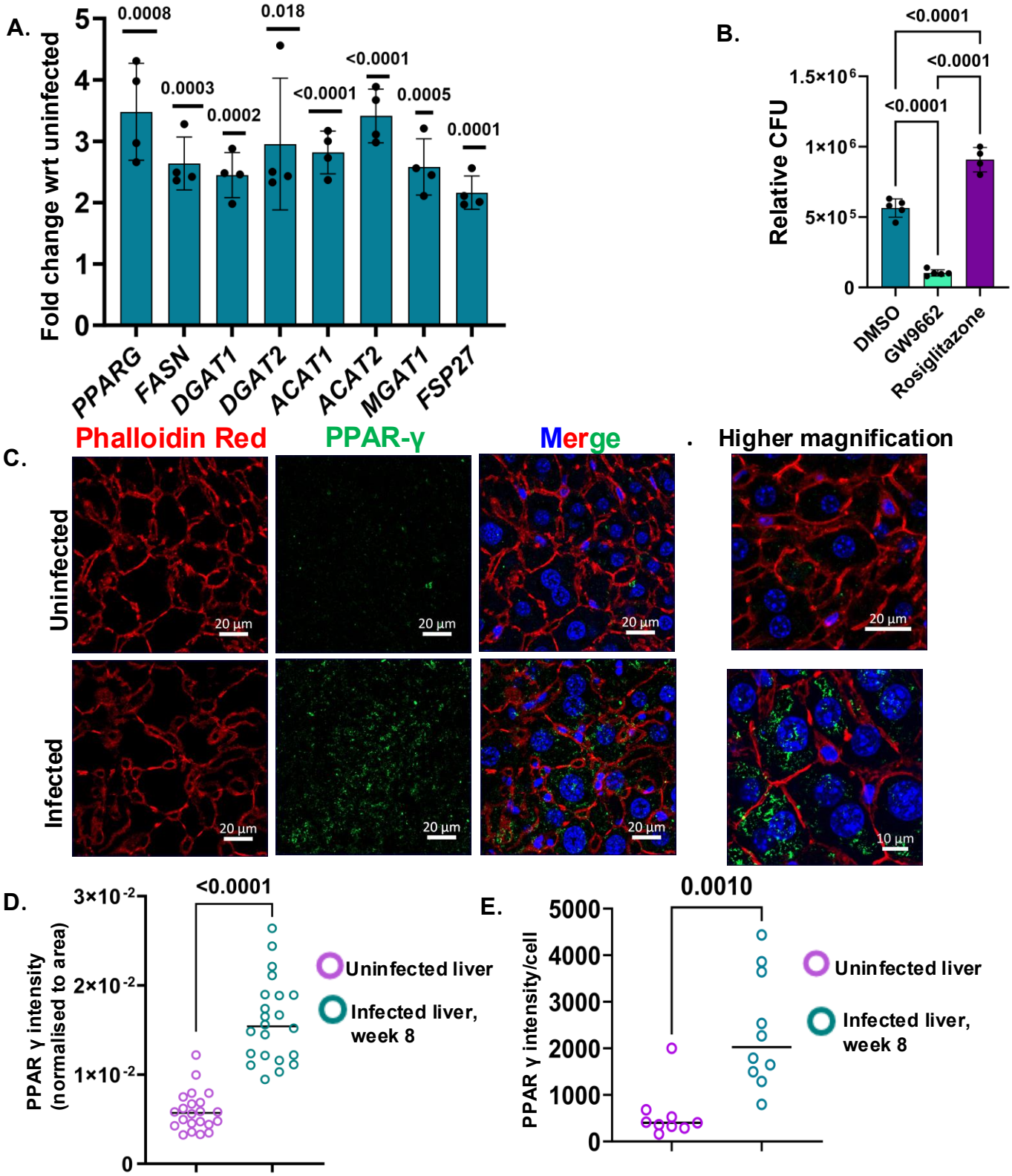

Figure 9, Supplementary

A.

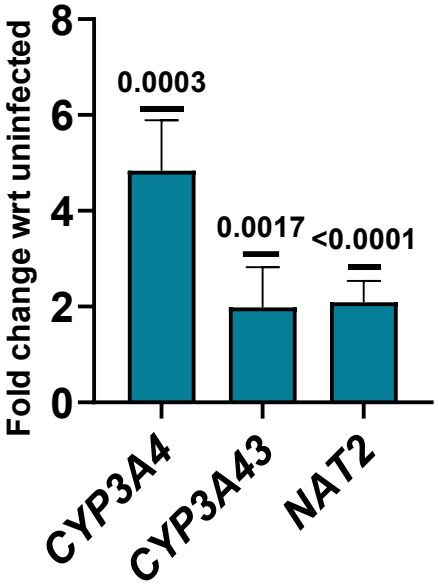

B.

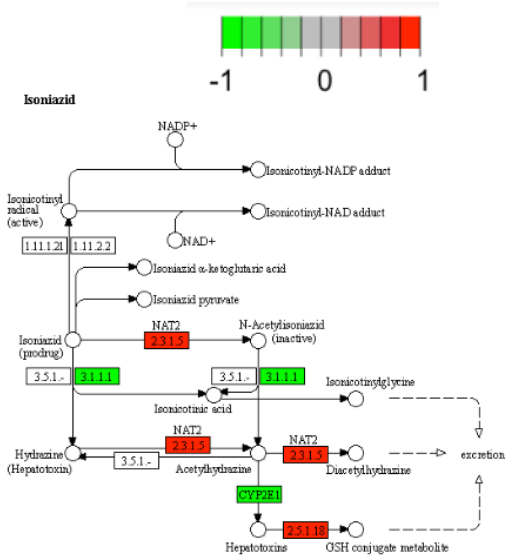

Figure 10 ,Supplementary

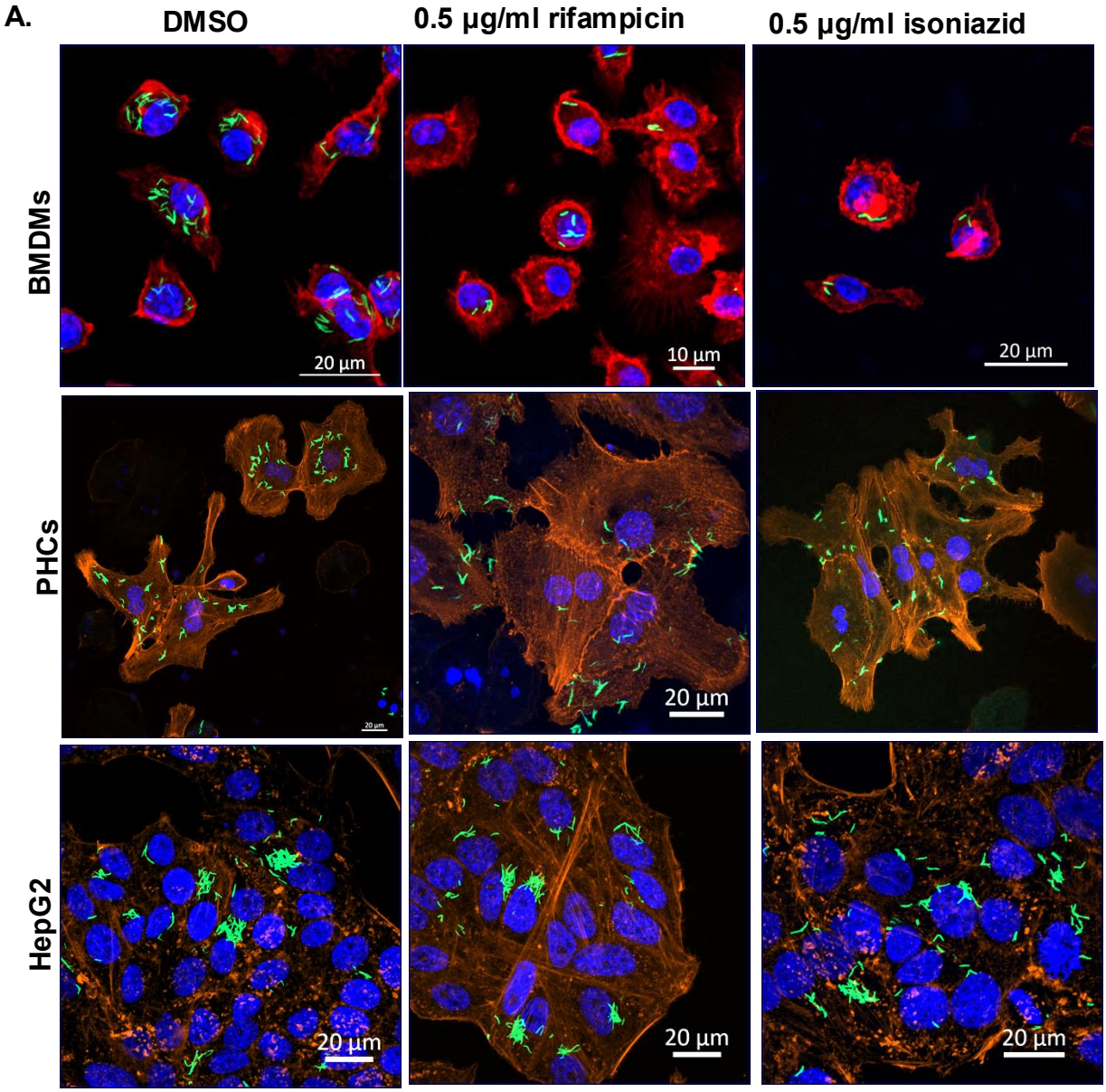

Figure 11,Supplementary

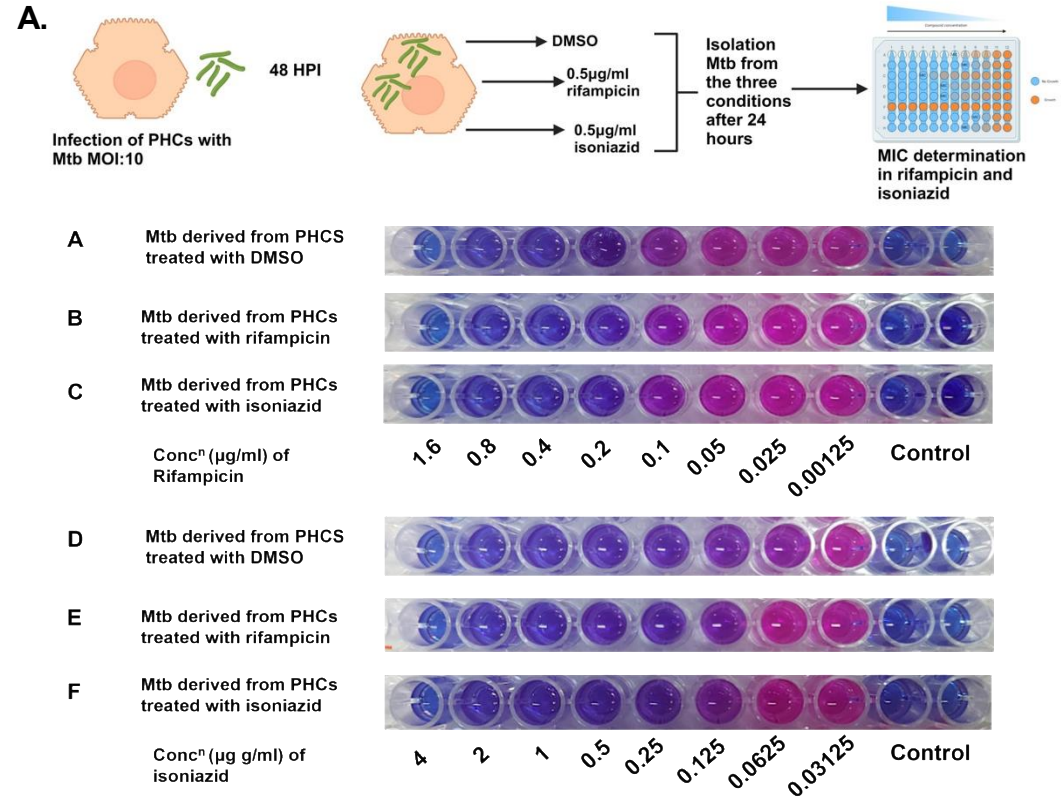

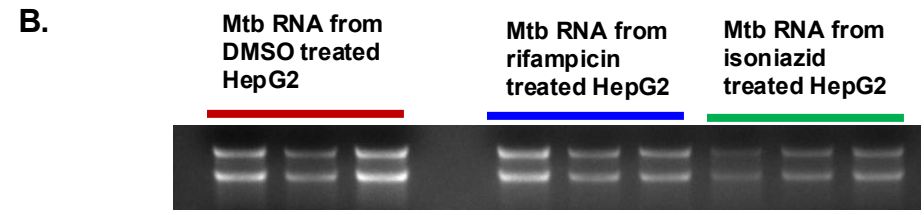

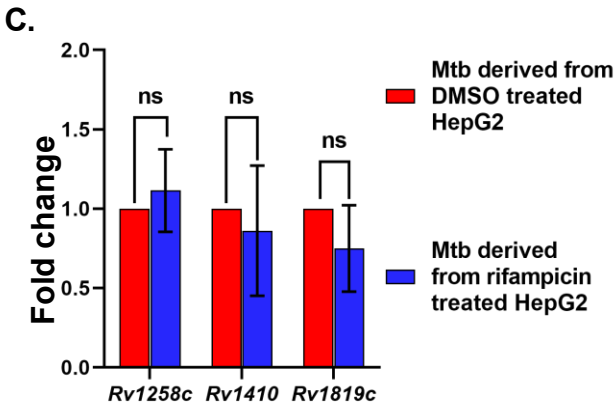

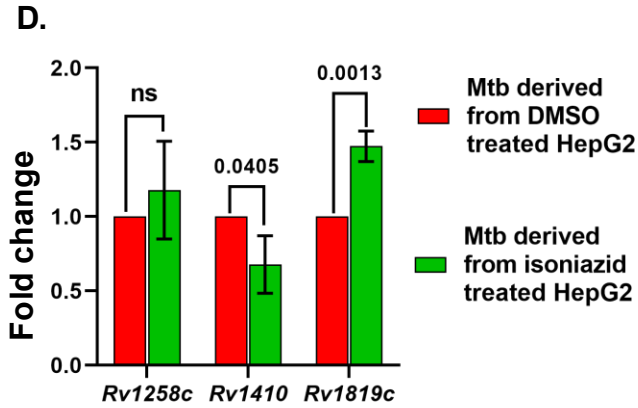

Figure 12 ,Supplementary

Supplementary Figure legends:

Figure S1: Histopathological changes in the liver biopsy samples of miliaryTB patients: (A and B): A-O staining and FISH in the liver biopsy of the uninfected (control) group shows no Mtb-specific signals. **(C).** H & E staining shows enhanced immune cell infiltration in the liver biopsy of the pulmonary TB patients compared to the uninfected control. **(D).** Dual staining of β-actin (green) and Ag85B (red) using respective antibodies shows the presence of Mtb in hepatocytes and other cells in liver biopsy sections (indicated by yellow arrows) **(E).** H&E staining shows distinct granuloma in the lung section of pulmonary TB patient and **(F).** Acid-fast staining in the same lung section shows a high bacterial load **(G).** A-O staining in the same lung section further validates the presence of high Mtb load. Scale bars in A, B and C are 50 µm and in D is 20 µm. and E and F are 150 µm. Data shown in this figure is representative of 5 patients with pulmonary TB.

Figure S2: Histopathological changes in the murine liver post Mtb infection: (A).10^5 number of H37Rv were administered intra-peritoneally (IP) and the bacterial burden was enumerated in primary hepatocytes that were isolated from the infected mice. **(B).** Analysis of the serum parameters of albumin, ALT, AST and GGT in the uninfected and infected mice at the mentioned time points, mice were infected through the aerosol route with 200 CFU. **(C).** Representative H and E-stained liver sections show enhanced immune cell infiltration in Mtb-infected mice. **(D).** Multiplex immunostaining of infected mice liver with CD 45.2 and Ag85B indicates the presence of Ag85B positive signals in CD 45.2 cells. Sample size (n)= 5/6 mice in each group.

FigureS3: Involvement of the liver in the guinea pig aerosol infection model: (A). Guinea pigs were infected with 200 CFU of H37Rv through the aerosol route and the bacterial burden of the lungs, liver and spleen was enumerated at different time points post-infection **(B).** H and E images of the lung and the liver at 4- and 8-weeks post infection showing distinct granulomas in both the organs. Sample size (n)= 3 guinea pigs in each group.

Figure S4; Standardization of multiplicity of infection (MOI) in PHCs and HepG2: (A). Confocal microscopic images of Phalloidin Alexa fluor 555 stained PHCs infected with different multiplicity of infection (MOI) of Mtb-H37Rv-GFP. **(B).** Quantification of % infectivity at different MOIs in primary hepatocytes (PHCs) **(C).** Quantification of %

infectivity at different MOIs in HepG2. Relative CFU of Mtb in **(D).** HepG2, **(E).** PHCs**, (F).** RAW 264.7, **(G).** THP-1, **(H).** murine BMDMs at the respective time points post-infection.

Figure S5: Comparison of significant pathways between Mtb infected THP-1 and HepG2, 48 HPI: (A). GO pathway enrichment analysis was done for DEGs with adjusted p-value < 0.05 at 48 hours post-infection for Mtb-infected THP-1. (B). GO pathway enrichment analysis was done for DEGs with adjusted p-value < 0.05 at 48 hours post infection for Mtb-infected HepG2. The bubble plot depicts the enrichment of pathways on the mentioned time points post-infection, where the coordinate on the x-axis represents the gene ratio, the bubble size represents the gene count and colour represents the p value The bubble plot depicts the enrichment of pathways on the mentioned time points post-infection, where the coordinate on the x-axis represents the gene ratio, the bubble size represents the gene count and colour represents the p-value.

Figure S6: Increased lipid biogenesis provides a growth advantage to Mtb within hepatocytes: (A). Confocal microscopy showing the LDs in both PHCs and HepG2 under inhibitors of fatty acid biosynthesis and TAG biosynthesis. (B). Mtb RNA isolated from DMEM grown Mtb and HepG2-derived Mtb,48 HPI, with the RNA expression pattern of key lipid biogenesis genes and TAG biosynthesis genes in Mtb as determined by qRT PCR, the fold change has been calculated by considering the expression in the DMEM grown Mtb to be 1 (C). Experimental plan for metabolic labelling of Hepg2 and subsequent infection by Mtb (schematic of experimental procedure generated using Biorender.com) (D). Fluorescently labelled fatty acid (BODIPY 558/568 C12) staining in DMSO treated, C75 treated and T863 treated HepG2. Data were analyzed by using the two-tailed unpaired Student's t-test in B. *p < 0.05, **p < 0.005, ***p < 0.0005, ****p < 0.0001, ns=non-significant.

Figure S7: Confocal microscopy images showing the puncta of fluorescently labelled fatty acid (BODIPY558/568 C12) in Mtb isolated from metabolically labeled HepG2: (A). Confocal images showing puncta of labeled fatty acid in Mtb derived from DMSO, C75 and T863 treated metabolically labeled HepG2.

Figure S8: Enhanced lipid accumulation in the liver of Mtb infected mice: (A). BODPIY staining in the liver of the uninfected and 8 weeks post Mtb infected murine liver (B). Dual staining of BODIPY (green) and Ag85B (red) shows Ag85B colocalization with BODIPY (highlighted in the zoomed image). (C). Representative images showing the mean lipidTOX Neutral Red staining in infected liver, 2-, 4- and 8-weeks post infection (D). Plot depicting the mean lipidTOX intensity at the mentioned time points post-infection (normalized to the area. Data were analyzed one-way ANOVA. *p < 0.05, **p < 0.005, ***p < 0.0005, ****p < 0.0001. ns=nonsignificant in I. Representative data from experiments having n=4-6 mice/ group.

Figure S9: Mtb induced PPARγ expression in infected hepatocytes: (A). mRNA levels of PPARγ and other lipid biosynthetic genes in infected HepG2, the fold change has been calculated by considering the expression in the uninfected cell to be 1 (B). Relative bacterial burden in DMSO, GW9662 and rosiglitazone treated HepG2 infected with Mtb H37Rv. (C). Multiplex immunostaining showed increased expression of PPARγ in the liver of infected mice, 8 weeks post-infection. (D). Bar plot showing PPARγ intensity (normalized to the area) in the uninfected and infected liver, 8 weeks post-infection. (E). Intensity of PPARγ per hepatocyte in uninfected and infected liver, 8-week post-infection. Data were analyzed by using the two-tailed unpaired Student's t-test in (A, D, and E) and by one-way ANOVA in B. Representative data from n=4 biological replicates *$p < 0.05$, **$p < 0.005$, ***$p < 0.0005$, ****$p < 0.0001$. ns=non-significant.

Figure S10: Gene expression analysis of key DMEs related to rifampicin and isoniazid metabolism: (A). Relative expression of CYP3A4, CYP3A43, and NAT2 genes in infected HepG2 post-Mtb infection, the fold change has been calculated by considering the expression in the uninfected cells to be 1. Data were analyzed using the two-tailed unpaired Student's t test in C. *$p < 0.05$, **$p < 0.005$, ***$p < 0.0005$, ****$p < 0.0001$, ns=non-significant. (B). KEGG pathway analysis shows the upregulation of NAT2 gene (N-acetyltransferase 2) in Mtb infected HepG2

Figure S11: Microscopic images of Mtb infected BMDMs, PHCs and HepG2 treated with rifampicin and isoniazid: (A). Confocal microscopy images of Mtb-H37Rv-GFP infected BMDMs, PHCs, and HepG2. All the cells are treated with DMSO, 0.5 µg/ml rifampicin, and 0.5 µg/ml isoniazid post-infection. The cells were stained with Phalloidin Alexa fluor-555 to demarcate the cell boundary. Representative data from 3 independent experiments. Each dot represents a single field having more than 4 infected cells.20 such fields were analyzed. Figure

Figure S12: Mtb derived from hepatocytes show no changes in drug efflux pumps and antibiotic sensitivity: (A). Resazurin microtitre assay of the three groups of Mtb in different concentrations of isoniazid and rifampicin (schematic of experimental procedure generated using Biorender.com). (B). Mtb was obtained from DMSO-treated, 0.5 µg/ml rifampicin, and 0.5 µg/ml isoniazid-treated HepG2 by differential lysis and RNA was isolated from those Mtb populations (C and D). qRT-PCR of some of the key efflux pumps genes in these three Mtb groups. Data were analysed using the two-tailed unpaired Student's t-test in C and D. *$p < 0.05$, **$p < 112\ 0.005$, ***$p < 0.0005$, ****$p < 0.0001$, ns=non-significant.